Article

Amazonia as a carbon source linked to deforestation and climate change

🔵 Check for updates

Luciana V. Gatti[1,2 ✉], Luana S. Basso[1], John B. Miller[3], Manuel Gloor[4], Lucas Gatti Domingues[1,2,5], Henrique L. G. Cassol[1], Graciela Tejada[1], Luiz E. O. C. Aragão[1,6], Carlos Nobre[7], Wouter Peters[8,9], Luciano Marani[1], Egidio Arai[1], Alber H. Sanches[1], Sergio M. Corrêa[1,10], Liana Anderson[11], Celso Von Randow[1], Caio S. C. Correia[1,2], Stephane P. Crispim[1] & Raiane A. L. Neves[1]

Amazonia hosts the Earth's largest tropical forests and has been shown to be an important carbon sink over recent decades[1–3]. This carbon sink seems to be in decline, however, as a result of factors such as deforestation and climate change[1–3]. Here we investigate Amazonia's carbon budget and the main drivers responsible for its change into a carbon source. We performed 590 aircraft vertical profiling measurements of lower-tropospheric concentrations of carbon dioxide and carbon monoxide at four sites in Amazonia from 2010 to 2018[4]. We find that total carbon emissions are greater in eastern Amazonia than in the western part, mostly as a result of spatial differences in carbon-monoxide-derived fire emissions. Southeastern Amazonia, in particular, acts as a net carbon source (total carbon flux minus fire emissions) to the atmosphere. Over the past 40 years, eastern Amazonia has been subjected to more deforestation, warming and moisture stress than the western part, especially during the dry season, with the southeast experiencing the strongest trends[5–9]. We explore the effect of climate change and deforestation trends on carbon emissions at our study sites, and find that the intensification of the dry season and an increase in deforestation seem to promote ecosystem stress, increase in fire occurrence, and higher carbon emissions in the eastern Amazon. This is in line with recent studies that indicate an increase in tree mortality and a reduction in photosynthesis as a result of climatic changes across Amazonia[1,10].

The Amazon forest contains about 123 ± 23 petagrams carbon (Pg C) of above- and belowground biomass[11], which can be released rapidly and may thus result in a sizeable positive feedback on global climate[12]. Additionally, deforestation and forest degradation reduce Amazonia's capacity to act as carbon sink. Hydrologically, Amazonia is one of the three major air upwelling regions in the tropics, and the rainforest receives basin-wide rainfall averaging around 2,200 mm yr^{-1}. Amazonia exhibits complex relationships between ecosystem carbon and water fluxes and climate[13,14]. For example, evapotranspiration has been estimated by several studies to be responsible for 25% to 35% of total rainfall[14–16]. Large-scale human disturbance of these ecosystems can be expected to alter these ecosystem–climate interactions. Over the past 40 to 50 years, human impact has increasingly affected Amazonia, resulting in a forest loss of around 17%, of which 14% has been converted mostly to agricultural land (89% pasture and 10% crops)[17]. Removal of forests causes an increase in temperature[13,18–20] and reduces evapotranspiration, and has been shown to reduce precipitation downwind of deforested areas[6,14,21]. Furthermore, regional

deforestation and selective logging lead to the degradation of adjacent forests, which increases their vulnerability to fires, promoting further degradation[4,13,22]. These effects are further enhanced by temperature increases caused by a decrease in forest cover[6,7] and are superimposed on the backdrop of global warming.

Atmospheric carbon vertical profiles

A large-scale integrating indicator of the state of an ecosystem is its greenhouse gas balance, mainly the carbon balance. Here, we report CO_2 fluxes between 2010 and 2018 using almost 600 CO_2 (Extended Data Fig. 1a) and CO aircraft vertical profiles (VPs) that provide the responses of Amazonian ecosystems to direct human impact and regional climate change. Figure 1 shows the regions of influence and the location of four vertical profiling sites. Profiles extend from near the surface to approximately 4.5 km above sea level and are collectively sensitive to surface fluxes from a large fraction of Amazonia. The air arriving at our sampling sites comes predominantly from the east, with the north–south component

[1]General Coordination of Earth Science (CGCT), National Institute for Space Research (INPE), São José dos Campos, Brazil. [2]Nuclear and Energy Research Institute (IPEN), São Paulo, Brazil. [3]Global Monitoring Laboratory, National Oceanic and Atmospheric Administration (NOAA), Boulder, CO, USA. [4]School of Geography, University of Leeds, Leeds, UK. [5]National Isotope Centre, GNS Science, Lower Hutt, New Zealand. [6]College of Life and Environmental Sciences, University of Exeter, Exeter, UK. [7]Institute of Advanced Studies (IEA), University of São Paulo (USP), São Paulo, Brazil. [8]Department of Meteorology and Air Quality, Wageningen University, Wageningen, The Netherlands. [9]Centre for Isotope Research, University of Groningen, Groningen, The Netherlands. [10]Rio de Janeiro State University (UERJ), Resende, Brazil. [11]National Center for Monitoring and Early Warning of Natural Disasters (CEMADEN), São José dos Campos, Brazil. ✉e-mail: luciana.gatti@inpe.br
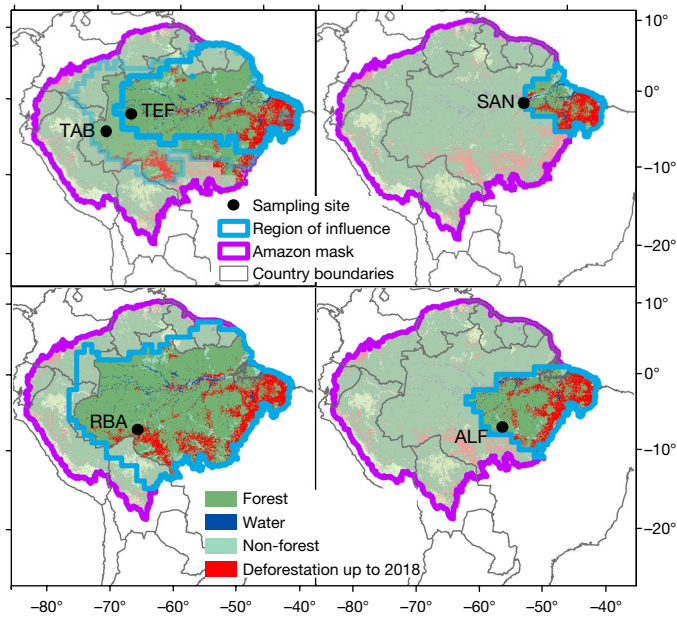
Fig. 1 | Regions of influence. Average regions of influence (2010–2018), delimited by light-blue lines according to the density of HYSPLIT back-trajectories (see Methods and Extended Data Fig. 2c for details), inside the Amazon mask (purple line; $7.25 \times 10^6 \, km^2$) for each VP site: TAB_TEF (northwest; TAB, 2010–2012 and TEF, 2013–2018), SAN (northeast), ALF (southeast) and RBA (southwest). The aircraft VP sites are shown as black circles. Cumulative historical deforestation (red) data are from PRODES[32] only for the Brazilian Amazon up to 2018 (see Methods).

Fig. 2 | Annual mean VPs. Annual mean VPs for each site and year (2010–2018) constructed from the VP monthly mean (the background was subtracted from each height), giving ΔVP. The black lines represent the 2010–2018 mean VPs for each site. Vertically averaged values of ΔVP for each site and each year are shown in Extended Data Fig. 1c.

of the flow being dependent on the seasonally varying position of the Intertropical Convergence Zone (Fig. 1, Extended Data Fig. 2a). As a result, air samples collected at the four sites are influenced by regions with different levels of human disturbance (Fig. 1). Site-specific regions of influence were determined using air-mass back-trajectory calculations (Extended Data Fig. 2; see Methods). We use quarterly resolved regions of influence to determine the average spatially weighted magnitudes of potential carbon flux drivers, such as historical deforestation extent, temperature and precipitation, upwind of each site. Additionally, the regions of influence for each site are used to calculate spatially weighted mean fluxes for all of Amazonia (see Methods).

Annual mean VP CO_2 enhancements or depletions relative to background (ΔVP) (Extended Data Fig. 1b) are a function of the cumulative effect of all C sources and sinks between the Atlantic coast and each site. We examine ΔVP as a data-based diagnostic to gain a first-order understanding of C source and sink patterns. The annual mean ΔVP for each site (Fig. 2) is calculated by subtracting background CO_2 concentrations, determined from remote Atlantic Ocean surface sites, from CO_2 concentrations at each VP sampling height (see Methods); vertically averaged annual mean ΔVPs are also calculated (Extended Data Fig. 1c; see Methods). Figure 2 shows the annual and nine-year-mean ΔVP for the eastern sites SAN (northeastern Amazon; hereafter referred to as SAN-NE) and ALF (southeastern Amazon; hereafter ALF-SE) and the western sites RBA (southwestern-central Amazon; hereafter RBA-SWC) and TAB_TEF (northwestern-central Amazonia; hereafter TAB_TEF-NWC). Vertically averaged ΔVP values, which are proportional to surface flux, suggest that ALF-SE has the largest CO_2 emission to the atmosphere, followed by SAN-NE. By contrast, ΔVP values for the western sites RBA-SWC and TAB_TEF-NWC indicate near-neutral C balance or C sinks.

An alternative way of examining the VPs is to not subtract the background, but just consider the vertical differences between the top of the profiles (>3.8 km) and the portion below the planetary boundary layer (<1.5 km) (Extended Da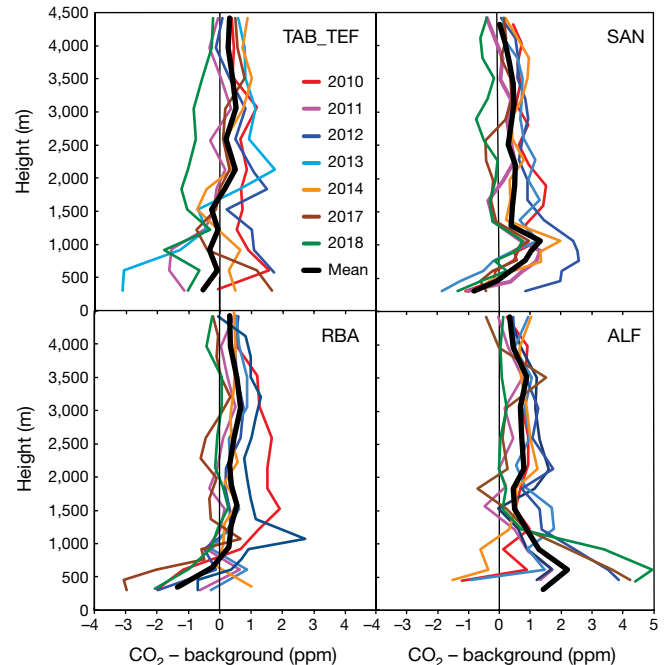ta Fig. 1d). As with the background subtraction approach, positive enhancements suggest a land source, whereas negative depletions suggest a sink. This vertical difference approach gives similar results to the background subtraction approach, indicating CO_2 emission to the atmosphere from the eastern sites (SAN-NE and ALF-SE) and almost neutral C balance or absorption of atmospheric CO_2 for the western sites (RBA-SWC and TAB_TEF-NWC). For ALF-SE the annual mean ΔVP values (Fig. 2) since the last strong El Niño (2015–2016) show higher CO_2 concentrations near the surface, representing an increase in emissions. Only RBA-SWC exhibits different behaviour between the two approaches, with near-neutral C balance implied by the background subtraction approach and apparent C uptake, on average, suggested by examining the annual mean vertical differences (Extended Data Fig. 1c, d). The annual mean RBA-SWC VP clearly shows the strongest carbon sink compared to the other regions; when considering only the vertical differences between >3.8 km and <1.5 km, the uptake from the surface is more evident. Long travel times of air masses from the coast to the VP sites enable more convection, promoting vertical mixing between the atmospheric layer that we measure and the layers above it. The result of such mixing is that some surface flux signal can be lost through the top of our measurement domain. In the case of CO, during the dry season we observe larger enhancements in the difference between >3.8 km and the background, indicating loss of signal, although CO plumes in particular are associated with pyro-convection and do not show a similar degree of signal loss for CO_2 (Supplementary Fig. 1). Vertical loss of signal is one of the sources of uncertainty that we account for in our approach (see Methods).

Regional Amazonian carbon fluxes

Partial column integrals of CO_2 from individual profiles are used to determine total carbon fluxes (FC_{Total}), which represent the result of all surface sources and sinks (natural and anthropogenic) between the coast and the sampling site. CO is used to determine the fraction of FC_{total} derived from biomass burning emissions (FC_{Fire}). By removing FC_{Fire} from FC_{Total},
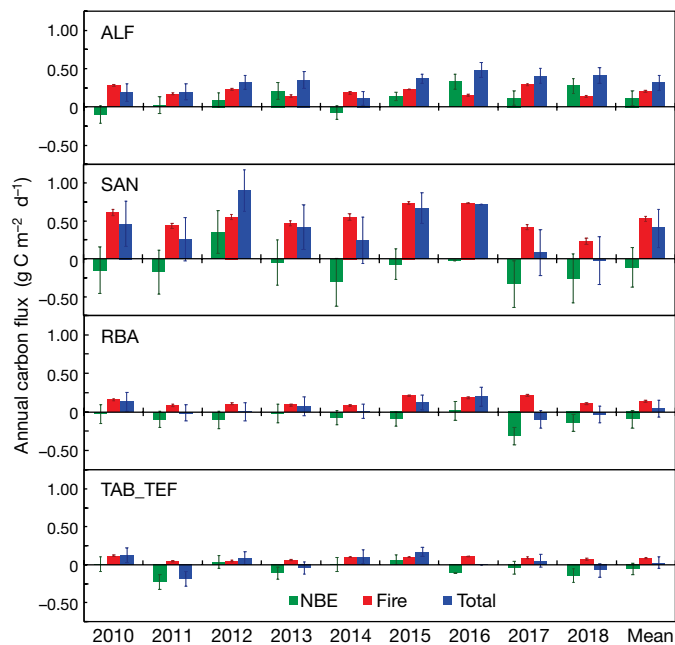
Fig. 3 | Annual carbon fluxes. Annual carbon fluxes for the regions upwind of SAN, ALF, RBA and TAB_TEF (TAB 2010–2012 and TEF 2013–2018). Blue bars show the total C flux, red bars denote fire C flux and green bars are NBE (total minus fire flux). Error bars are uncertainties related to the background and travel time trajectories for each sample used to compose first the monthly mean and later the annual means (see Methods).

we obtain the net biome exchange (FC_{NBE}) for the region upwind of a given VP (a negative NBE represents C sink). Total, fire and NBE carbon fluxes were combined into monthly, annual and long-term averages, and into east, west and basin-wide totals (Extended Data Table 2; see Methods).

For SAN-NE, the nine-year mean fluxes for FC_{Total}, FC_{Fire} and FC_{NBE} are 0.41 ± 0.25, 0.53 ± 0.03 and -0.11 ± 0.26 g C m^{-2} d^{-1}, respectively, where the uncertainties are based on background concentration and air parcel travel time (see Methods; Fig. 3, Extended Data Table 2). This region showed the highest carbon fluxes among our sites. The seasonality of carbon fluxes (Extended Data Figs. 3, 4) is the second largest for SAN-NE, as is true for the seasonality of precipitation, temperature and enhanced vegetation index (EVI; a measure of vegetation greenness; see Methods). ALF-SE shows the second highest FC_{Total} over nine years (0.32 ± 0.09 g C m^{-2} d^{-1}; Fig. 3) and exhibits the strongest seasonality for carbon fluxes, precipitation, temperature and EVI. Low EVI occurs in the dry season and can indicate a period of drier biomass (for example, leaf litter in the understory) with greater susceptibility to ignition. This region also includes the largest burned area (Extended Data Table 2). Over nine years, FC_{NBE} for this region shows a possible carbon source to the atmosphere ($+0.11 \pm 0.13$ g C m^{-2} d^{-1}), representing one-third of FC_{Total}. Seasonally, the region is a weak sink only during a part of the wet season, with most of the positive FC_{Total} in the dry season resulting from fire emissions and net respiration (Extended Data Fig. 3). We note, however, that part of the seasonality in fluxes observed for ALF-SE may result from the region of influence shifting southwards to areas of greater historical disturbance in the second and third quarters of the regions of influence (see section 'Climate trends and human impact'), which corresponds to the end of the wet season (April–May) and the dry season (June–September) (Extended Data Fig. 2a, b). During this part of the year, the Cerrado (savannah) biome to the south and east of the rainforest can represent about 40% in the second and third quarters of the region of influence (Extended data Fig. 2a). Over the nine years studied (2010–2018), the FC_{NBE} value for ALF-SE indicates that it is a steadily increasing source, at a rate of 0.036 ± 0.015 g C m^{-2} d^{-1} yr^{-1}

(Pearson's correlation, $r = 0.68$, $P = 0.045$) (Extended Data Fig. 5a). Between 2010 and 2018, annual FC_{Fire} averages 0.20 ± 0.01 g C m^{-2} d^{-1}. RBA-SWC, which has experienced less disturbance than the east, averaged a weak source over nine years ($FC_{Total} = 0.05 \pm 0.02$ g C m^{-2} d^{-1}), with FC_{NBE} an annual mean sink (-0.10 ± 0.02 g C m^{-2} d^{-1}), compensating about two-thirds of FC_{Fire} (0.14 ± 0.01 g C m^{-2} d^{-1}). The mean seasonal cycle of FC_{NBE} exhibits a wet season sink from November through March (Extended Data Fig. 3). RBA-SWC FC_{Fire} is high, largely because the 'arc of deforestation' is in the southern portion of the region, upwind of the site (Extended Data Fig. 2).

Air samples from TAB_TEF-NWC are sensitive to northwestern and central Amazonia, one of the regions least affected by human activities. VPs of CO_2 and CO were measured at TAB from 2010 to 2012, and at TEF from 2013 to 2018, but their regions of influence and flux seasonal cycles are very similar, so we have analysed them as a single time series (Supplementary Fig. 2 and Extended Data Fig. 4). Combining TAB and TEF, the nine-year mean FC_{Total} shows near-neutral C balance (0.03 ± 0.08 g C m^{-2} d^{-1}), with FC_{NBE} (-0.06 ± 0.08 g C m^{-2} d^{-1}) nearly compensating for fire emissions (0.08 ± 0.01 g C m^{-2} d^{-1}) (Extended Data Table 2). Seasonality in both FC_{Total} and FC_{NBE} is absent for TAB_TEF, with both FC_{Total} and FC_{NBE} having near-neutral C balance all year. This lack of seasonality may result from the near-absence of dry months (less than 100 mm of precipitation) in the upwind region, which is also expressed as low seasonal fire fluxes and burned area; EVI seasonality is also the smallest of all sites. Lack of EVI seasonality is related to a relatively high constant fraction of photosynthetically active radiation (fPAR) absorbed by plants, and thus a lower fraction of dry biomass throughout the year, reducing fire risk (Extended Data Figs. 3, 4).

CO_2 gradients from the annual mean VPs and the estimated carbon fluxes for these sites indicate a link between areas that are more affected by land use and cover change and higher carbon emissions to the atmosphere.

Considering the upwind areas of each site, we combine fluxes from all sites to calculate a total Amazonia carbon balance for our nine-year study period (see Methods) of 0.29 ± 0.40 Pg C yr^{-1} ($FC_{Total} = 0.11 \pm 0.15$ g C m^{-2} d^{-1}), where fire emissions represent 0.41 ± 0.05 Pg C yr^{-1} ($FC_{Fire} = 0.15 \pm 0.02$ g C m^{-2} d^{-1}), with NBE removing -0.12 ± 0.40 Pg C yr^{-1} (31% of fire emissions) from the atmosphere ($FC_{NBE} = -0.05 \pm 0.15$ g C m^{-2} d^{-1}). The east (region 1 in Extended Data Fig. 6), which represents 24% of Amazonia (of which 27% has been deforested), is responsible for 72% of total Amazonian carbon emissions, where 62% is from fires. One recent study showed cumulative gross emissions of carbon of about 126.1 Mg CO$_2$ ha^{-1} for 30 yr after a fire event, where cumulative CO$_2$ uptake from forest regrowth offsets only 35% of the emissions. Another recent study[13] reported that fire emissions from Amazonia are about 0.21 ± 0.23 Pg C yr^{-1}. Recently, van der Werf et al.[24] estimated for the period 1997–2009 that globally, fires were responsible for an annual mean carbon emission of 2.0 Pg C yr^{-1}, where about 8% appears to have been associated with South American forest fires, according to estimates from the Global Fire Emission Data set (GFED V.3). The Amazon Forest Inventory Network (RAINFOR) project showed a decline in sink capacity of mature forests due to an increase in mortality[1–3]. Adjusting the three RAINFOR studies to a consistent area (7.25×10^6 km^2) and taking their mean yields a basin-wide sink for intact forests of about -0.57, -0.41 and -0.23 Pg C yr^{-1} for 1990–1999, 2000–2009 and 2010–2019, respectively. The NBE from this study is consistent with the RAINFOR results for the last decade, because NBE represents the uptake from forest but also all non-fire emissions, such as decomposition, degradation and other anthropogenic emissions (see Supplementary Table 3).

Climate trends and human impact

The regions of influence for the four sites differ substantially with regard to human impact, in particular deforestation. Using site-specific regions
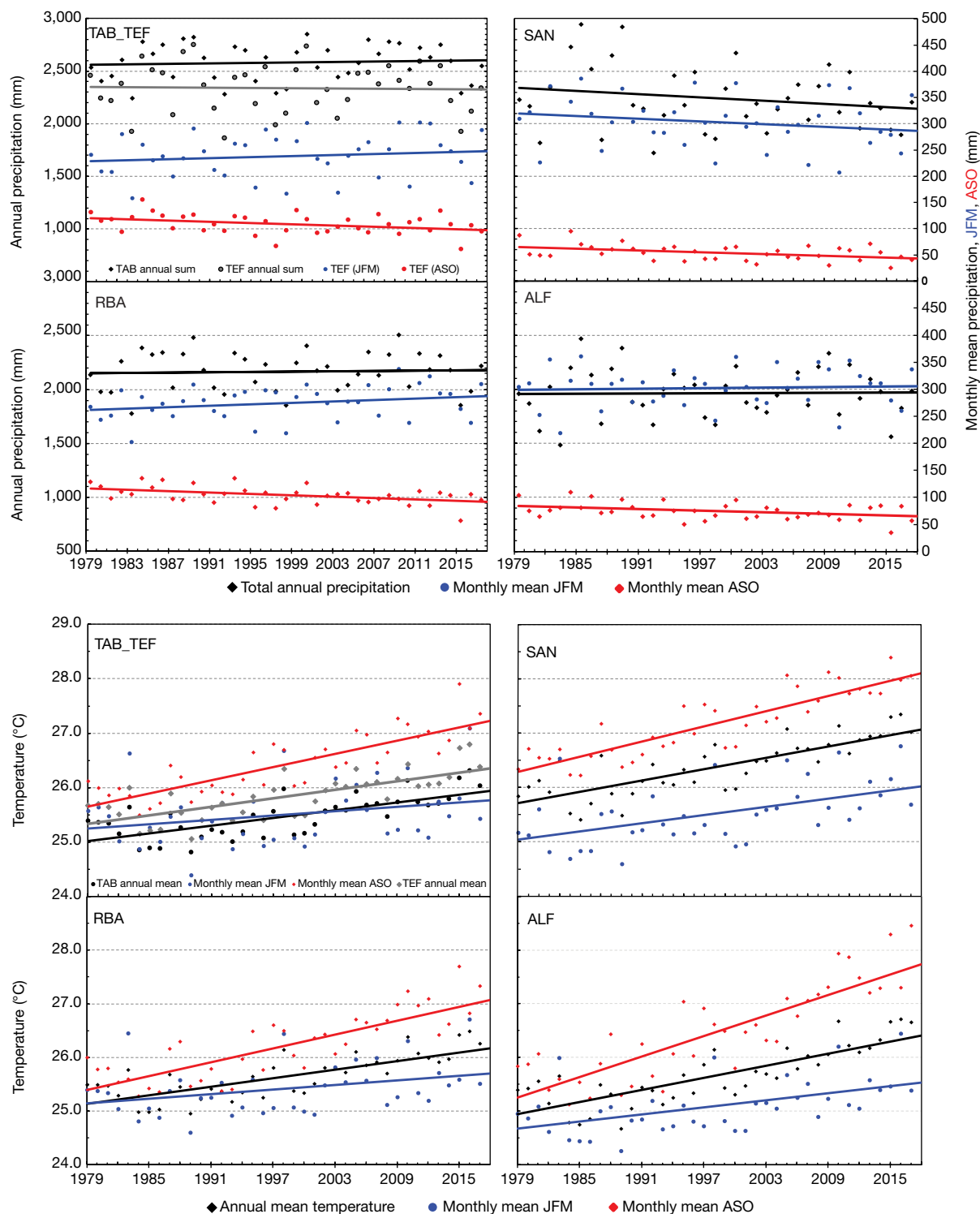
Fig. 4 | 40-year precipitation and temperature trends. Precipitation trends using GPCP V2.3 (upper panels) and temperature trends using ECMWF re-analysis (ERA)-Interim, from 1979 to 2018 (lower panels) for the four sites. Annual accumulated precipitation (black) and monthly mean precipitation for ASO (August, September and October; red) and JFM (January, February and March; blue). Mean annual, JFM and ASO temperature are shown using the same colours as for precipitation. For the TAB_TEF site, shown are annual precipitation and temperature trends for TAB (black) and TEF (grey). ASO and JFM values are shown only for TEF, because there is no dry season at TAB (see Methods).

of influence averaged over our nine-year study period (Extended Data Fig. 2c), we determine the cumulative historical deforestation fractions of the areas upwind of SAN-NE, ALF-SE, RBA-SWC and TAB_TEF-NWC to be 31%, 26%, 13% and 7%, respectively (see Methods). The SAN-NE and ALF-SE VPs sample air affected by yet higher levels of deforestation

during the second and third quarters of the year (Extended Data Fig. 2a, b). For SAN-NE, deforestation increases to 39% and 42%; for ALF-SE, it increases to 32% and 39%, respectively.

The regions of influence of eastern and western Amazonia sites also differ with regard to long-term climate trends. We found similar annual

mean warming trends for the whole Amazonia (1.02 ± 0.12 °C) as for the global mean (0.98 °C)[25] between 1979 and 2018 (see Methods). However, warming trends differ between months, and the largest increases were observed for the three dry-season months, August, September and October (ASO; 1.37 ± 0.15 °C). Annual mean precipitation did not change significantly (27 ± 68 mm; $P = 0.69$), but, similar to temperature trends, ASO precipitation decreased by 17%, enhancing the contrast between dry season and wet season (Extended Data Fig. 7, Extended Data Table 1).

Between 1979 and 2018 there are also considerable regional contrasts in temperature and precipitation trends, mainly in the dry season. Those for the eastern regions SAN-NE and ALF-SE, which have the largest fractions of historically deforested land, stand out; these are highly affected mainly by livestock and, to a lesser extent, by crops[17]. SAN-NE, 37% of which has been deforested, is the only region where annual mean precipitation has exhibited a statistically significant decrease in the past 40 years (9% or 208 ± 167 mm), with the largest reduction during ASO (34%) (Figs. 4, 5, Extended Data Table 1). Although annual mean precipitation upwind of ALF-SE did not change significantly (14 ± 36 mm; $P = 0.81$), ASO precipitation decreased by 24%, as noted previously for a similar region of Amazonia[6,7,26]. Although the fractional and absolute reduction rate in ASO precipitation for SAN-NE and ALF-SE is similar to those of the western sites (Extended Data Table 1), the impact of this drying on the ecosystems is probably greater, because dry-season moisture in the east was lower than in the west during the past four decades (Fig. 4, Extended Data Fig. 8). Temperature increases over 40 years for the eastern regions are also larger than for Amazonia as a whole: 1.38 ± 0.15 °C at SAN-NE and 1.46 ± 0.11 °C at ALF-SE annually, with increases of 1.86 ± 0.16 °C and 2.54 ± 0.29 °C, respectively, during ASO (Extended Data Fig. 8, Extended Data Table 1). Moreover, these changes appear to be accelerating, with annual grown rates increasing over the past 40, 30 and 20 years (Extended Data Table 1). For ALF-SE, temperature has also increased by 3.07 ± 0.29 °C for the two hottest months, August and September (Extended Data Fig. 8). These temperature and precipitation changes are also associated with a large positive trend in vapour pressure deficit in southeastern Amazonia[5], which suggests increasing plant stress. For ALF-SW, two factors are contributing to promote an increase in temperature: global climate change[5,8,21,27,28] and large-scale deforestation and forest degradation, amplifying these trends in this region.

The two western sites, RBA-SWC and TAB_TEF-NWC, also exhibit their strongest trends during the dry season. There was no significant annual mean change in precipitation for RBA-SWC (30 ± 104 mm; $P = 0.78$), but ASO precipitation dropped by 20% (Fig. 4). Its annual mean temperature increased similarly to global rates, although it was also largest during ASO (1.72 ± 0.15 °C). The relatively pristine region upwind of TAB_TEF-NWC (with 7% historical deforestation) also shows a decreasing trend of 20% in ASO precipitation, but no significant annual mean trend (23 ± 125 mm; $P = 0.85$) (Fig. 4, Extended Data Table 1). A possible reason for this 20% decrease in precipitation in both western-central regions, despite experiencing less deforestation compared to the eastern sites, is the cascade effect[14]. That is, deforestation in eastern Amazonia may be reducing evapotranspiration, which in turn may be reducing the recycling of water vapour that is transported to the western Amazonia. Annual mean temperature trends for TAB and TEF were similar to global trends, and although ASO temperature trends are larger than the annual mean, they are smaller than those of the other regions (Extended Data Table 1). The analysis of 40 years of temperature and precipitation data over Amazonia shows the relationship between deforestation extent and decreases in precipitation and increases in temperature, mainly during the dry season, with different trends observed for the eastern and western Amazonia.

Differences between eastern and western Amazonia

Dividing Amazonia into regions influencing eastern (SAN and ALF: region 1) and western (RBA and TAB_TEF: region 2) sites (Extended
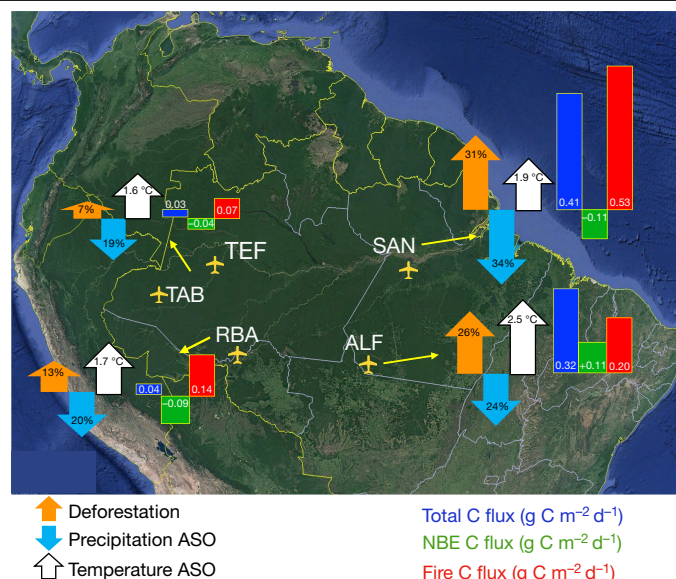

Fig. 5 | Spatial results overview. Summary of historical trends and fluxes for the regions upwind of each site: historical deforestation (orange arrows), reduction in precipitation during ASO (light blue arrows), increase in temperature in ASO (white arrows) and carbon fluxes (total, dark blue bars; NBE, green bars; fire, red bars). Base map from Google Earth (Image Landsat/Copernicus/USDSG; accessed 2020).

Data Fig. 6a) reveals notable differences. The east (region 1) represents approximately 1.6×10^6 km², with cumulative historical deforestation of approximately 27%. The west (region 2), on the other hand, has a much larger region of influence (approximately 4.1×10^6 km²) and a much smaller fraction of historically deforested land (11%). The eastern average annual mean $FC_{Total} = 0.35 \pm 0.11$ g C m^{-2} d^{-1}, $FC_{Fire} = 0.31 \pm 0.01$ g C m^{-2} d^{-1} and $FC_{NBE} = +0.04 \pm 0.11$ g C m^{-2} d^{-1} could be associated with historical deforestation and climate changes in the east (see Methods). The eastern averages are strongly influenced by southeastern Amazonia, represented by observations from ALF-SE, which is characterized by a positive FC_{NBE} (carbon emission), very strong dry-season temperature increases, precipitation decreases and large historical deforestation (Extended Data Tables 1, 2).

For ALF-SE, the relationship between moisture and temperature and FC_{NBE} and FC_{Fire} can be directly observed from our CO_2 and CO observations for the 2010–2018 period. The positive trend in NBE at ALF-SE correlates with the annual mean temperature and GRACE (equivalent water thickness) satellite soil water storage anomalies (see Methods) (multivariate linear correlation, $r = 0.88$, $P = 0.011$), suggesting that temperature and water availability in the soil have a significant impact on the vegetation carbon balance, at least in the southeast (Extended Data Figs. 3, 4, 5b). Interannual variations of FC_{Fire} for the ALF-SE region are strongly correlated with ASO (peak of dry season) temperature and precipitation ($r = 0.81$ and $r = -0.73$, respectively), showing that temperature and moisture affect both components of FC_{Total}. This region also exhibits almost twice the burned area of any other region (Extended Data Figs. 3, 4), and interannual burned area is highly correlated with FC_{Fire} ($r = 0.97$). Historically, eastern Amazonia has experienced a strong increase in dry-season temperature, reduced precipitation and increased duration[7–9,29,30], which together are creating an increasingly severe environment for vegetation, not only during extreme drought years, but every year, especially for the southeast[31].

By contrast, the regions influencing the western sites have experienced relatively lower levels of human disturbance and dry-season climate trends. For the regions upwind of TAB_TEF-NWC and RBA-SWC, we observed a near-neutral $FC_{Total} = 0.04 \pm 0.07$ g C m^{-2} d^{-1}, minimal fire emissions (0.11 ± 0.01) and a carbon sink of $FC_{NBE} = -0.08 \pm 0.07$ g C m^{-2} d^{-1}

(Extended Data Table 2). In a scenario in which the entire Amazonia has the same FC_{NBE} as western sites, the whole area would act as a sink of 0.20 Pg C yr^{-1}.

The east–west difference in total flux can be explained mainly on the basis of CO-based fire emissions and burned area (Fig. 5, Extended Data Table 2). However, the dry-season climate trends and the stronger historical deforestation and degradation in the east may make the area more susceptible to fire[13]. Historical land use change and climate trends may also explain the higher (positive) FC_{NBE}, especially in the southeast. A recent study pointed out that after 30 years, burned area still is a CO_2 source to the atmosphere, of which 73% resulted from subsequent tree mortality and decomposition[23]. This decomposition emission could not be compensated by CO_2 uptake by photosynthesis. For undisturbed forests, increasing temperatures and moisture stress may increase tree mortality[1–3,10] and negatively affect photosynthetic C uptake by trees via a decline in photosynthetic capacity[30]. Moreover, higher air temperatures generally lead to higher rates of soil carbon decomposition in both intact forests and disturbed land. Trends of regional climate and land disturbance over the past 40 years in Amazonia may be connected. The spatial correspondence of these trends with carbon fluxes between 2010 and 2018 suggest that such interactions may have long-term effects on the Amazonian C balance.

Online content

Any methods, additional references, Nature Research reporting summaries, source data, extended data, supplementary information, acknowledgements, peer review information; details of author contributions and competing interests; and statements of data and code availability are available at https://doi.org/10.1038/s41586-021-03629-6.

1. Brienen, R. J. W. et al. Long-term decline of the Amazon carbon sink. *Nature* **519**, 344–348 (2015).
2. Phillips, O. L. & Brienen, R. J. W. Carbon uptake by mature Amazon forests has mitigated Amazon nations' carbon emissions. *Carbon Balance Manag.* **12**, 1 (2017).
3. Hubau, W. et al. Asynchronous carbon sink saturation in African and Amazonian tropical forests. *Nature* **579**, 80–87 (2020).
4. Gatti, L. V. et al. Drought sensitivity of Amazonian carbon balance revealed by atmospheric measurements. *Nature* **506**, 76–80 (2014).
5. Barkhordarian, A., Saatchi, S. S., Behrangi, A., Loikith, P. C. & Mechoso, C. R. A recent systematic increase in vapor pressure deficit over tropical South America. *Sci. Rep.* **9**, 15331 (2019).
6. Leite-Filho, A. T., de Sousa Pontes, V. Y. & Costa, M. H. Effects of deforestation on the onset of the rainy season and the duration of dry spells in southern Amazonia. *J. Geophys. Res. Atmos.* **124**, 5268–5281 (2019).
7. Fu, R. et al. Increased dry-season length over southern Amazonia in recent decades and its implication for future climate projection. *Proc. Natl Acad. Sci. USA* **110**, 18110–18115 (2013).
8. Tan, P. H., Chou, C. & Tu, J. Y. Mechanisms of global warming impacts on robustness of tropical precipitation asymmetry. *J. Clim.* **21**, 5585–5602 (2008).
9. Spracklen, D. V., Arnold, S. R. & Taylor, C. M. Observations of increased tropical rainfall preceded by air passage over forests. *Nature* **489**, 282–285 (2012); corrigendum **494**, 390 (2013).
10. Doughty, C. E. et al. Drought impact on forest carbon dynamics and fluxes in Amazonia. *Nature* **519**, 78–82 (2015).
11. Malhi, Y. et al. The regional variation of aboveground live biomass in old-growth Amazonian forests. *Glob. Change Biol.* **12**, 1107–1138 (2006).
12. Cox, P. M., Betts, R. A., Jones, C. D., Spall, S. A. & Totterdell, I. J. Acceleration of global warming due to carbon-cycle feedbacks in a coupled climate model. *Nature* **408**, 184–187 (2000); erratum **408**, 750 (2000).
13. Aragão, L. E. O. C. et al. 21st Century drought-related fires counteract the decline of Amazon deforestation carbon emissions. *Nat. Commun.* **9**, 536 (2018).
14. Staal, A. et al. Forest-rainfall cascades buffer against drought across the Amazon. *Nat. Clim. Chang.* **8**, 539–543 (2018).
15. Costa, M. H. & Foley, J. A. Trends in the hydrologic cycle of the Amazon Basin. *J. Geophys. Res. Atmos.* **104**, 14189–14198 (1999).
16. Aragão, L. E. O. C. The rainforest's water pump. *Nature* **489**, 217–218 (2012).
17. Proyecto MapBiomas Amazonía. Colección [2.0] de los mapas anuales de cobertura y uso del suelo. *Mapbiomas_Amazonia* http://amazonia.mapbiomas.org/mapas-de-la-coleccion (2020).
18. Baker, J. C. A. & Spracklen, D. V. Climate benefits of intact Amazon forests and the biophysical consequences of disturbance. *Front. For. Glob. Change* **2**, 47 (2019).
19. Almeida, C. T., Oliveira-Júnior, J. F., Delgado, R. C., Cubo, P. & Ramos, M. C. Spatiotemporal rainfall and temperature trends throughout the Brazilian Legal Amazon, 1973–2013. *Int. J. Climatol.* **37**, 2013–2026 (2017).
20. Marengo, J. A. et al. Changes in climate and land use over the Amazon region: current and future variability and trends. *Front. Earth Sci.* **6**, 228 (2018).
21. Costa, M. H. & Pires, G. F. Effects of Amazon and Central Brazil deforestation scenarios on the duration of the dry season in the arc of deforestation. *Int. J. Climatol.* **30**, 1970–1979 (2010).
22. Nobre, C. A. et al. Land-use and climate change risks in the amazon and the need of a novel sustainable development paradigm. *Proc. Natl Acad. Sci. USA* **113**, 10759–10768 (2016).
23. Silva, C. V. J. et al. Estimating the multi-decadal carbon deficit of burned Amazonian forests. *Environ. Res. Lett.* **15**, 114023 (2020).
24. van der Werf, G. R. et al. Global fire emissions and the contribution of deforestation, savanna, forest, agricultural, and peat fires (1997–2009). *Atmos. Chem. Phys.* **10**, 11707–11735 (2010).
25. NASA/GISS. *Global Climate Change, Global Temperature* https://climate.nasa.gov/vital-signs/global-temperature/ (accessed 6 March 2020).
26. Maeda, E. E. et al. Evapotranspiration seasonality across the Amazon Basin. *Earth Syst. Dyn.* **8**, 439–454 (2017).
27. Haghtalab, N., Moore, N., Heerspink, B. P. & Hyndman, D. W. Evaluating spatial patterns in precipitation trends across the Amazon basin driven by land cover and global scale forcings. *Theor. Appl. Climatol.* **140**, 411–427 (2020).
28. Leite-Filho, A. T., Costa, M. H. & Fu, R. The southern Amazon rainy season: the role of deforestation and its interactions with large-scale mechanisms. *Int. J. Climatol.* **40**, 2328–2341 (2020).
29. Esquivel-Muelbert, A. et al. Compositional response of Amazon forests to climate change. *Glob. Change Biol.* **25**, 39–56 (2019).
30. Liu, J. et al. Contrasting carbon cycle responses of the tropical continents to the 2015–2016 El Niño. *Science* **358**, eaam5690 (2017).
31. Alkama, R. & Cescatti, A. Biophysical climate impacts of recent changes in global forest cover. *Science* **351**, 600–604 (2016).
32. INPE. *Amazon Deforestation Monitoring Project (PRODES)* http://www.obt.inpe.br/OBT/assuntos/programas/amazonia/prodes (2019).

Article

Methods

Sites, air sampling and analysis

The Amazon study area was defined according to subregions from Eva et al.[33] and biomes from Olson et al.[34]. For the Amazon mask we considered the four subregions: Amazon sensu stricto, Andes, Guiana and Gurupi, yielding a total study area of 7,256,362 km^2. We excluded the Planalto subregion because it is outside the tropical and subtropical moist broadleaf forest biome (Supplementary Fig. 4).

Measurements at the four Amazonian aircraft VP sites of the CARBAM project started in 2010 for SAN (2.86° S 54.95° W), ALF (8.80° S 56.75° W), RBA (9.38° S 67.62° W); in 2010–2012 for TAB (5.96° S 70.06° W); and in 2013 for TEF (3.39° S 65.6° W). The sampling rate was typically twice per month. Over nine years, 590 VPs were performed (Extended Data Fig. 1a, b) in a descending spiral profile from 4,420 m to 300 m above sea level (a.s.l.). An average of 75 VPs were performed per year from 2010 to 2018 at the four sites, except for 2015 and 2016. In 2015 the data collection flights were stopped in April at all sites, returning only in November at RBA. In 2016, profiles were performed only at RBA and ALF. The VPs were usually taken between 12:00 and 13:00 local time. Air was sampled by semi-automatic filling of 0.7-l boro-silicate flasks inside purpose-built suitcases[35]; two versions were used: one with 17 flasks used at SAN, and another with 12 flasks used at TAB_TEF, ALF and RBA. The flask suitcase is connected to a compressor package containing batteries, which is connected to an air inlet on the outside of the aircraft on the wing or the pilot's window, depending on the aircraft model (Supplementary Fig. 5). Air samples were analysed by a non-dispersive infrared analyser for CO_2 and by gas chromatography with HgO reduction detection for CO. The detailed analytical methods have been presented elsewhere[4]. To ensure accuracy and precision, we analysed the CO_2 mole fraction from 'target tanks' (calibrated CO_2 in air in high-pressure cylinders treated as unknowns) and demonstrated long-term repeatability of 0.02 ppm and a difference between measured and calibrated values of 0.03 ppm (ref. [36]).

Annual mean VPs

We calculated annual mean partial column averages from our VPs as a simple way to assess the robustness of our annual fluxes. For each site, annual mean profiles were calculated, starting with individual profiles and then averaging to monthly and annual values (Extended Data Fig. 1b). We also constructed the annual mean VPs by subtracting the background values at each altitude of each VP (ΔVP) to produce the annual mean enhancement or depletion at each altitude (Fig. 2). The air-density-weighted column mean was then calculated and compared to the annual mean flux calculated from the same profiles (Extended Data Fig. 1e). For all sites, we observed a high positive correlation between the column means and fluxes, suggesting that at least at the annual mean level, our fluxes—which incorporate more detail, such as travel time—are consistent with a simpler interpretation of the data.

Carbon flux estimation

Fluxes for each VP were calculated using a column budget technique that is based on the difference between trace gas concentration at the sites and the corresponding background values for each flask (ΔX) and the travel time of air parcels along the trajectory from the coast to the site (t) (equation (1)). Detailed information can be found in Gatti et al.[4], and this approach was also used by Miller et al.[37], Gatti et al.[38], Basso et al.[39] and D'Amelio et al.[40].

$$F_x = \int_{z=0 \text{ a.g.l.}}^{4.4 \text{ km a.s.l.}} \frac{\Delta X}{t(z)} dz. \tag{1}$$

To apply equation (1), we convert the measured mole fractions (in μmol CO_2 per mol of dry air; that is, ppm) to concentrations (mol CO_2 m^{-3})

using the density of air, where the temperature (T) and pressure (P) were measured during the VPs. When T and P were not measured, they were estimated using the equations derived for temperature and pressure using all measured T and P values relating to height for each site (equations (2)–(9)), where x is the altitude in metres, starting from the surface (0 m above ground level, a.g.l.) up to a height of 4.4 km a.s.l., T is expressed in degrees Celsius and P in mbar.

$$\text{SAN temperature } y = 1.9586x^2 - 249.49x + 5{,}815, \ r^2 = 0.97 \tag{2}$$

$$\text{SAN pressure } y = 0.0024x^2 - 12.46x + 11{,}069, \ r^2 = 0.87 \tag{3}$$

$$\text{ALF temperature } y = 0.4202x^2 - 170.62x + 5{,}201, \ r^2 = 0.89 \tag{4}$$

$$\text{ALF pressure } y = 0.0059x^2 - 20.21x + 14{,}402, \ r^2 = 0.87 \tag{5}$$

$$\text{RBA temperature } y = 0.1985x^2 - 167.77x + 4{,}953, \ r^2 = 0.97 \tag{6}$$

$$\text{RBA pressure } y = 0.0079x^2 - 21.10x + 13{,}872, \ r^2 = 0.89 \tag{7}$$

$$\text{TAB temperature } y = 2.415x^2 - 253.98x + 5{,}542, \ r^2 = 0.95 \tag{8}$$

$$\text{TAB pressure } y = 0.0051x^2 - 18.87x + 13{,}828, \ r^2 = 0.87. \tag{9}$$

For assigning background concentrations, we use the geographical position of each air-mass back-trajectory when it intersects two virtual limits. The first one is a latitude limit, from the Equator southwards at 30° W, and the second segment is a line from the Equator to the NOAA Global Monitoring Laboratory (NOAA/GML) observation site at Ragged Point, Barbados (RPB). The atmospheric air circulation over Amazonia is characterized by trade-wind easterlies coming from the tropical Atlantic Ocean[37] and moving west towards the Andes. This behaviour allows us to relate the position where an air mass crosses the virtual line with the concentrations measured at remote sites in the Atlantic—RPB, Ascension Island, UK (ASC) and Cape Point, South Africa (CPT)—from NOAA/GML to determine the background. This method was presented in Domingues et al.[41] (Supplementary Fig. 6).

To estimate travel times (t; equation (1)) we calculate back-trajectories for each air sampling level for each flight. 13-day backward trajectories are derived from the online version of the HYSPLIT model[42]. Then, the time when the back-trajectory crosses the coast is calculated with a resolution of 1 h. Mean travel times (2010–2018) from the coast to the sites are: SAN, 2.4 ± 1.5 days; ALF, 5.0 ± 2.0 days; RBA, 6.6 ± 2.1 days; TAB (2010–2012), 5.9 ± 1.9 days; and TEF, 4.9 ± 2.0 days. For each height interval, we calculate the associated flux and then sum them to obtain the flux estimate for each measured VP. To calculate annual means, we first calculate monthly mean fluxes (typically with two fluxes per site per month) and then average them.

Fire flux estimation

To estimate fluxes due to biomass burning, we used measured CO concentrations as a biomass burning tracer. We estimated CO:CO_2 fire emission ratios from clearly identifiable plumes in the VPs during the dry season, typically from August to December[4]. Average CO:CO_2 ratios were calculated by site (in units of parts per billion (ppb) CO per ppm CO_2): ALF CO:CO_2 = 53.4 ± 9.9 (1σ variability), based on 16 VPs; SAN CO:CO_2 = 55.5 ± 14.7, using 19 VPs; RBA CO:CO_2 = 73.2 ± 15.1, based on 12 VPs; and TAB_TEF CO:CO_2 = 71.6 ± 17.2, using 5 VPs. The two eastern sites exhibited lower ratios than the western sites. The eastern sites are sensitive to more deforested and degraded land, and are also influenced by the Cerrado and Caatinga biomes. The western sites are sensitive to more preserved areas and have a higher representativity

of Amazonia[43]. TAB_TEF represents a pristine area with much fewer biomass burning events.

Equation (10) was used to estimate CO_2 emissions from biomass burning. F_{CO} is the total CO flux and is calculated identically to CO_2 fluxes according to equation (1). To isolate the biomass burning flux from the total CO flux, we subtract the 'natural' CO flux, $F_{CO}^{natural}$, arising from direct soil CO emissions, and mainly CO from oxidation of volatile organic compounds (VOCs), such as isoprene that is emitted from the forest. Basin-wide average $F_{CO}^{natural}$ between the surface and 600 mbar (the approximate maximum altitude of the VPs) was calculated for 2010 and 2011, starting with output from the IMAGESv2 chemical transport model of the Belgian Institute for Space Aeronomy (BIRA). The VOC production in the model was tuned to HCHO (formaldehyde) observations from the GOME-2 and OMI satellites[44], resulting in improved estimates of atmospheric CO production from VOCs. These modelled fluxes were then adjusted on a site-by-site basis with a constant offset each year to match the mean total CO flux observed in the late wet season and the transition to the dry season, which in past studies[4,36] was taken to be equal to the year-round biogenic CO flux (late wet season and early dry season is March–June; except for SAN, for which March is excluded, because high CO fluxes are sometimes observed). 2010 fluxes were applied to all the dry years (2010, 2015, 2016) and 2011 fluxes were applied to all the wet years (2011–2014, 2017–2018). Observed, natural (modelled) and natural (adjusted) CO fluxes for 2010–2018 are shown in Supplementary Fig. 7. This biomass burning CO flux ($F_{CO} - F_{CO}^{natural}$) was then converted to biomass burning CO_2 flux (FC_{Fire}) using the observed CO_2:CO emission ratios discussed above ($R_{CO_2:CO}$) on a site-by-site basis (equation (10)). NBE represents the result of emissions and uptake from all processes in the influenced area for a specific VP, monthly and annual mean, excluding fire C emissions (NBE = total − fire).

$$FC_{Fire} = R_{CO_2:CO}(F_{CO} - F_{CO}^{natural}). \tag{10}$$

Regions of influence
We define regions of influence as those areas covered by the set of back-trajectories calculated from each VP and altitude, integrated on an annual and a quarterly basis per site. Annual regions of influence are the average areas throughout the series upwind of the VP per site (Fig. 1, Extended Data Fig. 2c). We developed a method[43] that uses individual back-trajectories for each sample in each VP, calculated by the HYSPLIT trajectory model[42,45] at a resolution of 1 h using $1° × 1°$ GDAS meteorology. For each site, all the back-trajectories in a quarter (January, February and March; April, May and June; July, August and September; October, November and December) or the whole year are binned, and the number of instances (at 1 h resolution) of back-trajectories between 300 to 3,500 m a.s.l. passing over a $1° × 1°$ grid cell is counted to determine the trajectory density (d_i) in each grid cell; that is, the density of trajectories from a single location and height that pass over a grid cell ($1° × 1°$) from 300 to 3,500 m a.s.l. We consider a cut-off of 3,500 m owing to three observations: first, plume rise associated with biomass burning rarely exceeds 3,500 m a.s.l.; second, mole fractions of CO_2 and other gases observed above 3,500 m a.s.l. are very similar to gas mole fractions from measurements in the tropical Atlantic marine boundary layer, which indicates minimal Amazonian surface influence; and third, changing the upper altitude limit from 3,500 m to 1,300 m (typical planetary boundary layer height) has minimal impact on our results. A back-trajectory may intersect a grid cell once or multiple times. The annual region of influence is defined by those grid cells with trajectories passing through them falling within the Amazon mask and further excluding grid cells associated with the lowest 2.5% of distribution of d_i (blue lines in Extended Data Fig. 2b). Note that back-trajectories for 'missing' VPs (that is, gaps in the data record) are calculated so that there are always trajectories for two VPs per month,

six per quarter and 24 per year. The mean annual regions of influence (Fig. 1, limited to just the Amazon mask, and Extended Data Fig. 2c) were determined by averaging the nine annual regions of influence for each site, using the sum of the number of points (frequency) within each grid cell integrating all VPs in the year (24 VPs per site) and then averaging over all nine years[43].

Quarterly region of influence
Quarterly regions of influence are maps of 'weighted trajectory density', w_i; that is, maps of trajectory density, d_i, divided by the sum of all densities over South American land (equation (11), where k is the number of all land grid cells) (Extended Data Fig. 2a, b, limited to the Amazonia mask). There are seasonal differences in circulation patterns, where the first and fourth quarters receive contributions from the Northern Hemisphere when the Intertropical Convergence Zone lies below the Equator, and in the second and third quarters when air masses always have origins south of the Equator, producing important differences in the regions of influence throughout the year[43].

$$w_i = \frac{d_i}{\sum_{i=1}^{k} d_i}. \tag{11}$$

Weighted mean
We used maps of w_i as spatial weighting functions for all studied parameters (temperature, precipitation, EVI, burned area, historical deforestation, and GRACE) to determine how each parameter influenced the carbon flux.

Temperature
We used 2-m temperatures from ERA-Interim that are monthly means of daily means obtained from the European Centre for Medium-Range Weather Forecasts (ECMWF; https://www.ecmwf.int/en/forecasts/datasets/reanalysis-datasets/era-interim)[46]. Monthly data are available since 1979 and were used with a resolution of $1° × 1°$ latitude–longitude. For the 40-year study we used maps of quarterly mean weights, w_i, averaged from 2010 to 2018, to determine the mean temperature upwind of each site (Fig. 4, Extended Data Figs. 7, 8, Extended Data Table 1). For comparison with the VPs from January 2010 to December 2018 (Extended Data Figs. 3, 4), we used trajectory-based weights corresponding to the specific quarter (for example, 2010 JFM, 2010 AMJ).

Precipitation
We used the databased GPCP (http://eagle1.umd.edu/GPCP_ICDR/GPCP_Monthly.html), version 2.3 (described by Adler et al.)[47] and version 1.3 (described by Huffman et al.)[48]. Version 2.3 represents monthly mean global precipitation since 1979 with a resolution of $2.5° × 2.5°$ latitude–longitude, and was used for the 40-year analysis (Fig. 4, Extended Data Figs. 7, 8, Extended Data Table 1). Version 1.3 contains daily data since 1996 with a resolution of $1° × 1°$ latitude–longitude, and was used for comparison with calculated carbon fluxes (Extended Data Figs. 3, 4).

Validation of temperature and precipitation data
The GPCP and ERA-Interim data products were validated using 35 automatic meteorological field stations for rainfall and temperature data from INMET (National Institute of Meteorology of Brazil), covering the periods 1996–2018 and 1979–2018, respectively. Precipitation from GPCP was also validated by Santos et al.[49]. In our study, a least-squares regression analysis was carried out by using the GPCP and ERA-Interim data as the dependent variable and the data from the automatic meteorological field stations as the independent variable. The GPCP and ERA-Interim dataset explained 62–94% and 16–93% of the rainfall and temperature variability captured by the automatic meteorological field stations, respectively (Supplementary Fig. 8). The root-mean-square error (r.m.s.e.) for the entire region was estimated to be ±68.22 mm

and ±1.19 °C, but it is not homogeneous in the study area, varying from ±49.5 mm to ±99.5 mm and from ±0.82 °C to ±2.99 °C for rainfall and temperature, respectively.

GRACE

For equivalent water thickness, we used the JPL (Jet Propulsion Laboratory) monthly land mass grids, which contain the land water mass anomaly given as equivalent water thickness, derived from GRACE (Gravity Recovery and Climate Experiment) time-variable gravity observations at 1.0° × 1.0° resolution[50]. For more details, see Landerer & Swenson[51].

Burned area

The burned area was obtained from the Moderate Resolution Imaging Spectroradiometer (MODIS) Collection 6 MCD64A1 burned area product[52]. Collection 6 provides monthly tiles of burned area with 500-m spatial resolution over the globe with an overall accuracy of 97% (ref. [52]). The algorithm uses several parameters for detecting burned area from the Terra and Aqua satellite products, such as a daily active fire (MOD14A1 and Aqua MYD14A1), daily surface reflectance (MOD09GHK and MYD09GHK) and annual land cover (MCD12Q1)[53–55]. The updated algorithm has the advantages of better detection of small fires (26% increase) and also reducing the temporal reporting accuracy from 68% within 2 days after the active fire[52]. The burned area product was resampled to 1° × 1° spatial resolution using the fraction of area burned in that grid cell and summing for each quarter using IDL/ENVI.

EVI

EVI is the enhanced vegetation index that aims to highlight the fraction of absorbed fPAR from terrestrial vegetation targets, similar to the normalized difference vegetation index (NDVI). In general, high positive values show a higher proportion of fPAR, and therefore greater vegetation greenness (vegetation vigour). EVI can also reveal the seasonality of different vegetation types, where tree individuals partly lose leaves during the dry season and become drier, thus reducing the index value. Unlike NDVI, EVI includes a blue band that minimizes the influence of aerosols and other adjustments to improve signal-to-noise ratio. Moreover, in high-leaf-area-index environments such as the Amazon, NDVI can saturate, whereas EVI does not. EVI is computed following equation (12) (ref. [56]):

$$EVI = G\frac{(NIR - Red)}{(NIR + C1Red - C2 \times Blue + L)},\tag{12}$$

where NIR (near-infrared; 0.841–0.876 μm), Red (0.62–0.67 μm) and Blue (0.459–0.479 μm) are the atmospherically corrected surface reflectance bands from MODIS; L is the correction of radiative transfer gain between NIR and Red in the canopy $L = 1$; $C1$ and $C2$ are the aerosol correction terms for NIR and Red, respectively, with $C1 = 6$ and $C2 = 7.5$; and G is the gain factor, $G = 2.5$. The EVI product used was the MANVI: MODIS multiangle implementation of atmospheric correction (MAIAC) nadir–solar adjusted vegetation indices for South America, generated at a spatial resolution of 1 km and a temporal resolution of 16 days[57].

Deforestation

Deforestation was calculated inside the Amazon mask for the whole Amazon and for each region of influence using the annual mean region of influence (Fig. 1) and quarterly mean regions of influence (Extended Data Fig. 2) from 2010 to 2018. The deforestation data were from the deforestation monitoring programme PRODES of INPE[32] (2015), which has measured the annual and official deforestation (larger than 6.25 ha) rate in the Brazilian Legal Amazon since 1988[58]. We normalized the trajectory density of the different influence areas and calculated the weighted deforestation (see Methods section 'Weighted mean').

Missing-data imputation

Missing monthly data for total, fire and NBE C fluxes at ALF, SAN, RBA, TAB_TEF are shown in red in Supplementary Fig. 9, owing to sampling and laboratory logistical issues. To fill these gaps, we applied missForest, a nonparametric missing-value imputation using random forest methodology[59]. It is used to impute continuous and/or categorical data, mainly when the phenomena involved show complex interactions and nonlinear relations[60]. After each iteration of the method, the difference between the previous and the new imputed data matrix is assessed for all variables. To adjust the set parameters—such as the number of iterations, number of trees, number of variables randomly sampled at each split and others—all known monthly data for each site were used. We performed the imputation for the total C flux (FC_{Total}) and fire C flux (FC_{Fire}) separately[61]. To train the method, we used 85% of the following monthly variables, with the remaining 15% used for cross-validation: temperature, precipitation, EVI, burned area and GRACE. FC_{Fire}, FC_{Total}, and cross-validation calculations were performed 1,000 times, and the results are the mean values presented in Fig. 3, Extended Data Figs. 3, 4 for the missing months. Cross-validation was conducted with 15% of random known data for each site for both fire and total fluxes at each site. The normalized r.m.s.e. was below 0.0043 for all sites and fluxes. The r.m.s.e. values for the cross-validation statistics were 0.0064, 0.0253, 0.0047 and 0.0054 g C m^{-2} d^{-1} for total fluxes and 0.0013, 0.0029, 0.0011 and 0.0003 g C m^{-2} d^{-1} for fire fluxes at ALF, SAN, RBA and TAB_TEF, respectively. These values were used in our uncertainty calculations for months with missing fluxes. We used the missForest implementation for R language[62].

Uncertainty and Monte Carlo error propagation

For Monte Carlo error propagation, we take into account the uncertainties in the background concentration and in the air parcel travel time. For the separation of total fire fluxes and land vegetation fluxes unrelated to fire, we account for the uncertainty in emission ratios, CO total fluxes and natural CO flux. The uncertainty due to CO_2 measurement uncertainty (<0.1 ppm) is negligibly small. We use the r.m.s.e. of the difference between the top-of-profile mean concentration above 3.8 km and the background mean concentration for the same levels (Supplementary Fig. 1) to represent background uncertainty. This approach helps to account for uncertainties associated with the background uncertainties and possible losses of surface flux through the top of our measurement domain (4.4 km of altitude) due to vertical mixing. We estimate back-trajectory uncertainties based on a comparison between HYSPLIT and two additional models, the FLEXPART Lagrangian particle dispersion model[63] and the mesoscale model BRAMS[64], for all profiles of 2010 (Supplementary Fig. 10a). We consider the largest difference in mean profile travel time from HYSPLIT and the other two models using the r.m.s.e. values. For fluxes from fire we use the standard deviation of emission ratios at each site and account for the CO flux uncertainties (estimated as for the CO_2 fluxes), and consider the uncertainty in natural CO flux. All parameters used in the Monte Carlo error propagation are listed in Supplementary Fig. 10b. The theoretical uncertainty for the nine-year mean fluxes is defined in equation (13a), where sigma$_i$ is the annual mean flux uncertainty for a given site. However, this approach assumes that annual fluxes are uncorrelated. To be conservative, allowing for significant year-to-year correlation, we calculate the nine-year uncertainties as equation (13b).

$$\text{sigma} = \sqrt{\frac{\sum \text{sigma}_i^2}{9}},\tag{13a}$$

$$\text{sigma} = \frac{\sum \text{sigma}_i}{9}.\tag{13b}$$

Scaling fluxes to all of Amazonia

Because fluxes at the eastern and western sites are very different, we separate Amazonia into separate regions, for each year (Extended Data Fig. 6a), given the observed interannual variability. Region 1 combines the regions of influence of SAN and ALF; region 2 combines the regions of influence of RBA and TAB (2010 to 2012) and TEF (2013 to 2018), excluding region 1; region 3 is the remaining region not covered by regions 1 and 2. Fluxes for region 1 were calculated by averaging fluxes from SAN and ALF using the areas of each site's annual region of influence as weights (equation (14)). Fluxes for region 2 were also calculated by weighting the mean flux of RBA and TAB (2010–2012) and RBA and TEF (2013, 2018), using a similar equation to equation (14). Fluxes for region 3 were assumed to be the same as for region 2. Extended Data Figure 6 shows the results for all nine years for the three regions. The basin-wide carbon fluxes are then calculated by scaling the fluxes from each region by their areas. The carbon budget was calculated by equation (15), extrapolated to 365.25 days, and is related to the entire Amazonia (7,256,362 km^2).

$$FC_{region1} = \frac{(FC_{SAN} \times Area_{SAN}) + (FC_{ALF} \times Area_{ALF})}{Area_{SAN} + Area_{ALF}}, \quad (14)$$

$$
\begin{aligned}
Balance_{Am.} = &(FC_{region1} \times Area_{region1}) \\
&+ (FC_{region2} \times Area_{region2-region1}) \\
&+ (FC_{region2} \times Area_{region3}).
\end{aligned} \quad (15)
$$

Data availability

The CO_2 VP data that support the findings of this study are available from PANGAEA Data Archiving, at https://doi.org/10.1594/PANGAEA.926834. Source data are provided with this paper.

33. Eva, H. D. et al. *A Proposal for Defining the Geographical Boundaries of Amazonia; Synthesis of the Results from an Expert Consultation Workshop Organized by the European Commission in Collaboration with the Amazon Cooperation Treaty Organization.* Report No. 21808-EN (European Commission, 2005).
34. Olson, D. M. et al. Terrestrial ecoregions of the world: a new map of life on Earth. *Bioscience* **51**, 933–938 (2001).
35. Tans, P. P., Bakwin, P. S. & Guenter, D. W. A feasible Global Carbon Cycle Observing System: a plan to decipher today's carbon cycle based on observations. *Glob. Change Biol.* **2**, 309–318 (1996).
36. Marani, L. et al. Estimation methods of greenhouse gases fluxes and the human influence in the CO_2 removal capability of the Amazon Forest. *Rev. Virtual Química* **12**, 5 (2020).
37. Miller, J. B. et al. Airborne measurements indicate large methane emissions from the eastern Amazon basin. *Geophys. Res. Lett.* **34**, L10809 (2007).
38. Gatti, L. V. et al. Vertical profiles of CO_2 above eastern Amazonia suggest a net carbon flux to the atmosphere and balanced biosphere between 2000 and 2009. *Tellus B* **62**, 581–594 (2010).
39. Basso, L. S. et al. Seasonality and interannual variability of CH_4 fluxes from the eastern Amazon Basin inferred from atmospheric mole fraction profiles. *J. Geophys. Res. Atmos.* **121**, 168–184 (2016).
40. D'Amelio, M. T. S., Gatti, L. V., Miller, J. B. & Tans, P. Regional N_2O fluxes in Amazonia derived from aircraft vertical profiles. *Atmos. Chem. Phys.* **9**, 8785–8797 (2009).
41. Gatti Domingues, L. et al. A new background method for greenhouse gases flux calculation based in back-trajectories over the Amazon. *Atmosphere* **11**, 734 (2020).
42. Draxler, R. R. *HYSPLIT 4 User's Guide.* Technical Memorandum ERL ARL-230 (NOAA, 1999); https://www.arl.noaa.gov/wp_arl/wp-content/uploads/documents/reports/arl-230.pdf
43. Cassol, H. L. G. et al. Determination of region of influence obtained by aircraft vertical profiles using the density of trajectories from the HYSPLIT model. *Atmosphere* **11**, 1073 (2020).
44. Stavrakou, T. et al. How consistent are top-down hydrocarbon emissions based on formaldehyde observations from GOME-2 and OMI? *Atmos. Chem. Phys.* **15**, 11861–11884 (2015).
45. Stein, A. F. et al. NOAA's HYSPLIT atmospheric transport and dispersion modeling system. *Bull. Am. Meteorol. Soc.* **96**, 2059–2077 (2015).
46. Berrisford, P. et al. Atmospheric conservation properties in ERA-Interim. *Q. J. R. Meteorol. Soc.* **137**, 1381–1399 (2011).
47. Adler, R. et al. The Global Precipitation Climatology Project (GPCP) monthly analysis (New Version 2.3) and a review of 2017 global precipitation. *Atmosphere* **9**, 138 (2018).
48. Huffman, G. J. et al. Global precipitation at one-degree daily resolution from multisatellite observations. **2**, 36–50 (2001).
49. Santos, S. R. Q., Sansigolo, C. A., Neves, T. T. A. T. & Santos, A. P. Variabilidade sazonal da precipitação na Amazônia: Validação da série de precipitação mensal do GPCC. *Rev. Bras. Geogr. Física* **10**, 1721–1729 (2017).
50. Landerer, F. *JPL TELLUS GRACE Level-3 Monthly LAND Water-Equivalent-Thickness Surface-Mass Anomaly Release 6.0 in netCDF/ASCII/GeoTIFF Formats* https://podaac.jpl.nasa.gov/dataset/TELLUS_GRAC_L3_JPL_RL06_LND (2019).
51. Landerer, F. W. & Swenson, S. C. Accuracy of scaled GRACE terrestrial water storage estimates. *Wat. Resour. Res.* **48**, W04531 (2012).
52. Giglio, L., Boschetti, L., Roy, D. P., Humber, M. L. & Justice, C. O. The Collection 6 MODIS burned area mapping algorithm and product. *Remote Sens. Environ.* **217**, 72–85 (2018).
53. Vermote, E. F., El Saleous, N. Z. & Justice, C. O. Atmospheric correction of MODIS data in the visible to middle infrared: first results. *Remote Sens. Environ.* **83**, 97–111 (2002).
54. Justice, C. et al. An overview of MODIS Land data processing and product status. *Remote Sens. Environ.* **83**, 3–15 (2002).
55. Friedl, M. A. et al. MODIS Collection 5 global land cover: algorithm refinements and characterization of new datasets. *Remote Sens. Environ.* **114**, 168–182 (2010).
56. Huete, A. et al. Overview of the radiometric and biophysical performance of the MODIS vegetation indices. *Remote Sens. Environ.* **83**, 195–213 (2002).
57. Dalagnol, R., Wagner, F. H., Galvão, L. S., Oliveira, L. E. & Aragao, C. *The MANVI Product: MODIS (MAIAC) Nadir-Solar Adjusted Vegetation Indices (EVI and NDVI) for South America* https://zenodo.org/record/3159488#.YLeQtH4o_IU (2019).
58. de Almeida, C. A. et al. High spatial resolution land use and land cover mapping of the Brazilian Legal Amazon in 2008 using Landsat-5/TM and MODIS data. *Acta Amazon.* **46**, 291–302 (2016).
59. Jiang, N. & Riley, M. L. Exploring the utility of the random forest method for forecasting ozone pollution in SYDNEY. *Int. J. Environ. Sustain. Dev.* **1**, 245–254 (2015).
60. Stekhoven, D. J. & Buhlmann, P. MissForest–non-parametric missing value imputation for mixed-type data. *Bioinformatics* **28**, 112–118 (2012).
61. Junninen, H., Niska, H., Tuppurainen, K., Ruuskanen, J. & Kolehmainen, M. Methods for imputation of missing values in air quality data sets. *Atmos. Environ.* **38**, 2895–2907 (2004).
62. R Core Team. *R: A Language and Environment for Statistical Computing* http://www.R-project.org (R Foundation for Statistical Computing, 2018).
63. Stohl, A., Forster, C., Frank, A., Seibert, P. & Wotawa, G. The Lagrangian particle dispersion model FLEXPART version 6.2. *Atmos. Chem. Phys.* **5**, 2461–2474 (2005).
64. Freitas, S. R. et al. The Coupled Aerosol and Tracer Transport model to the Brazilian developments on the Regional Atmospheric Modeling System (CATT-BRAMS) – Part 1: model description and evaluation. *Atmos. Chem. Phys.* **9**, 2843–2861 (2009).

Extended Data Fig. 1 | VPs, time series and annual mean CO₂ concentrations.
**a**, Time series of mean VPs of the CO₂ mole fractions of the flasks below 1.5 km a.s.l. (red circles) and above 3.8 km a.s.l. (blue circles) for sites SAN, ALF, RBA and TAB_TEF (590 VPs) and the background sites RPB, ASC and CPT. **b**, Annual mean VPs for the four sites (annual mean per height; see Methods). **c**, Annual mean ΔVP (see Methods) for each site and year. **d**, Annual mean differences between mean CO₂ mole fractions below 1.5 km a.s.l. and means above 3.8 km a.s.l. for each site and year (see Methods). **e**, Partial column annual means plotted against annual mean fluxes, by site.
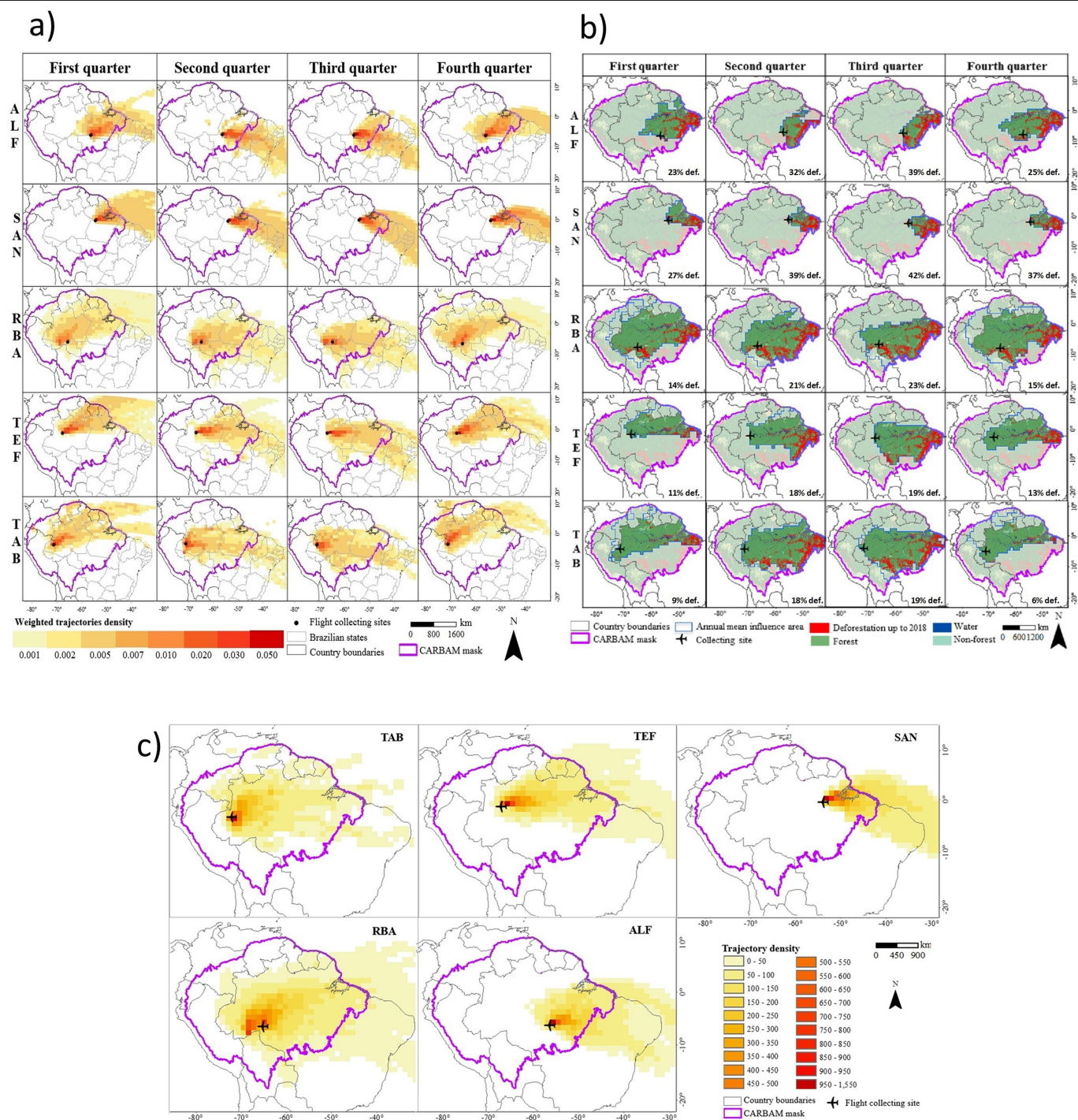
Extended Data Fig. 2 | Regions of influence. a, Mean quarterly regions of influence for the ALF, SAN, RBA, TEF and TAB sites, averaged between 2010 and 2018, calculated using the density of back-trajectories (see Methods). **b**, Deforestation inside quarterly regions of influence and the Amazon mask (purple line) using data from PRODES[32] (see Methods). **c**, Annual mean regions of influence (trajectory densities) averaged between 2010 and 2018.
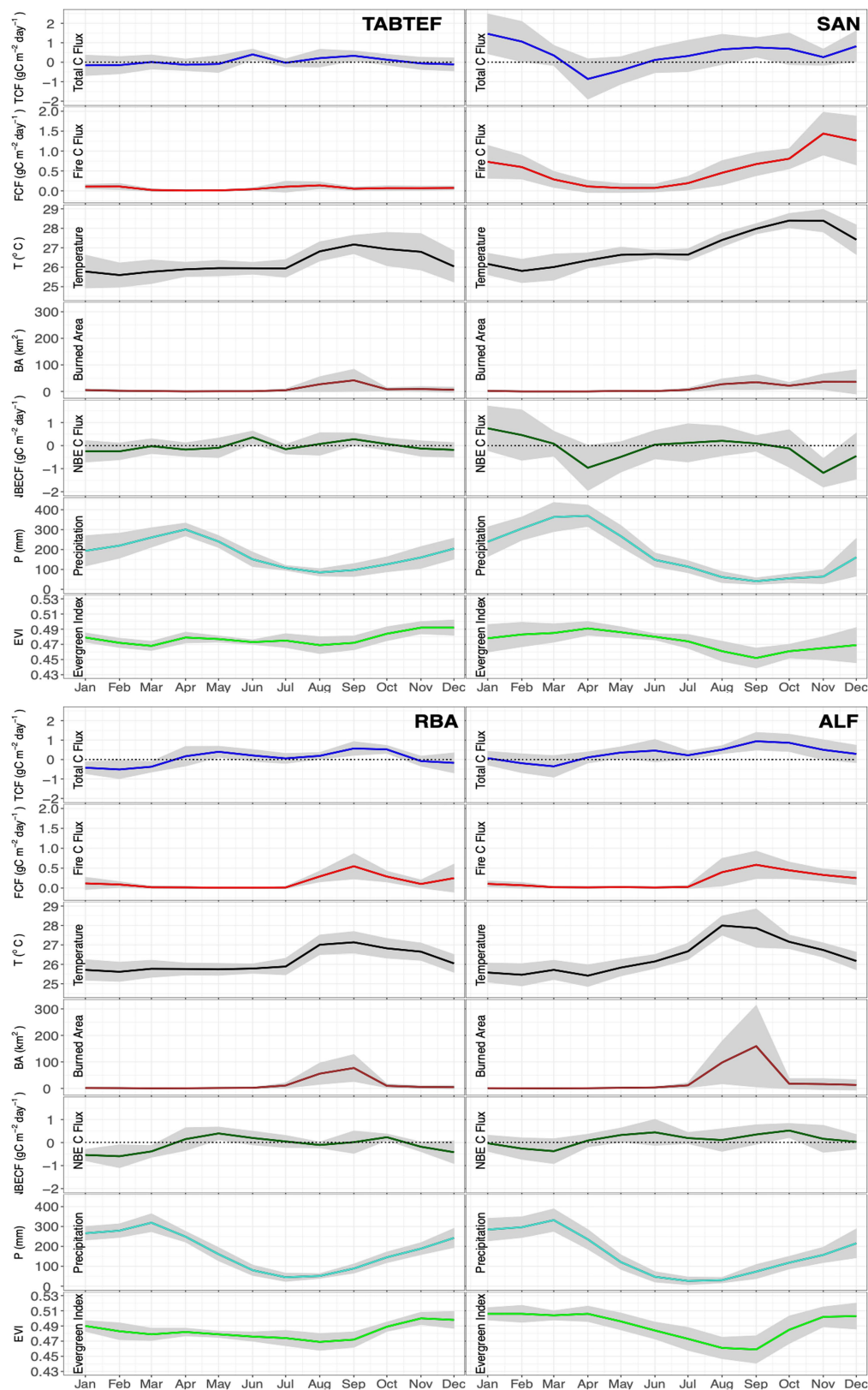
Extended Data Fig. 3 | Seasonal carbon flux and driver variables. Average monthly means of potential flux driver variables at sites TAB_TEF, SAN, RBA and ALF in 2010–2018. Grey bands denote the standard deviation of the monthly mean.
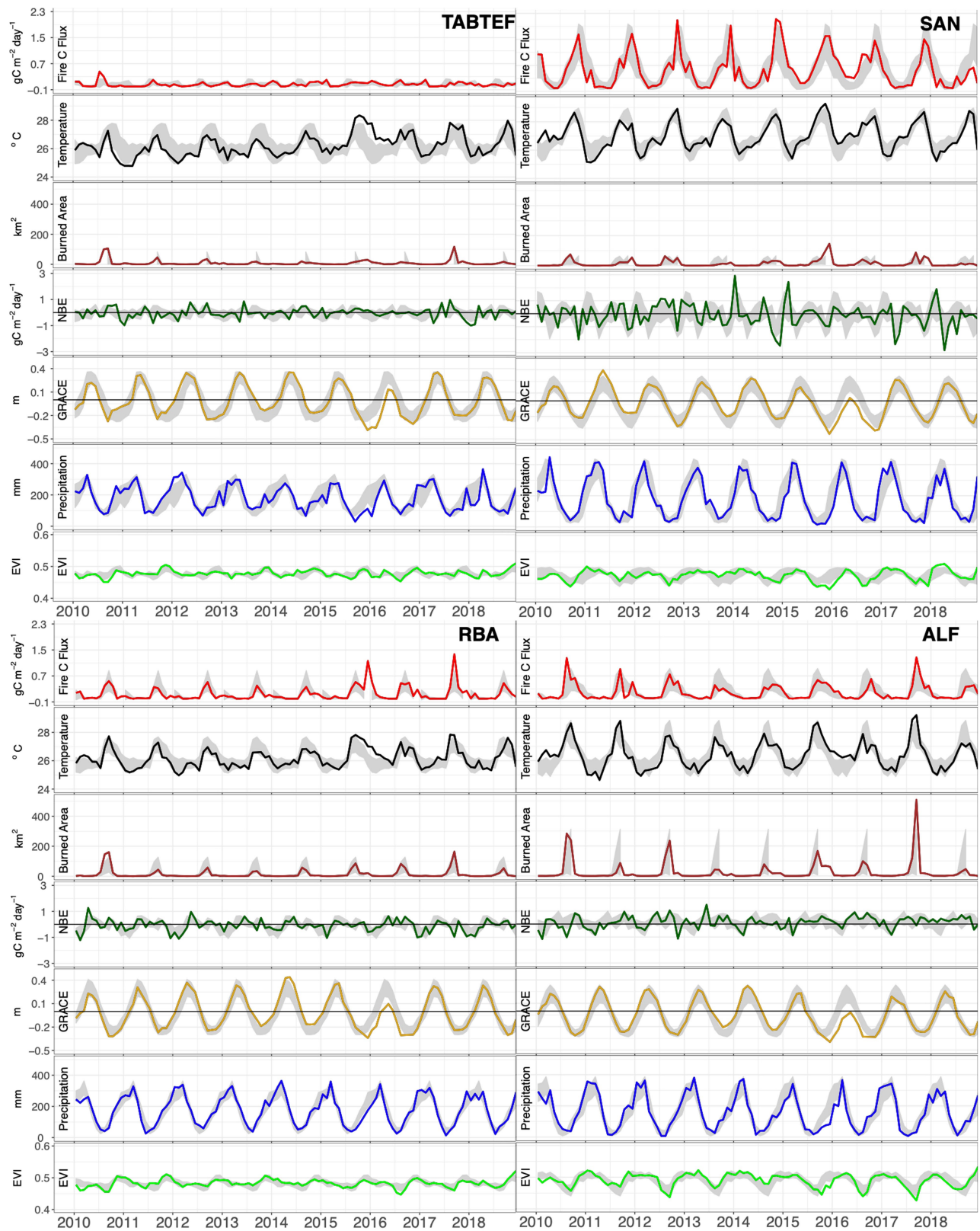
Extended Data Fig. 4 | Time series of carbon flux and driver variables. As in Extended Data Fig. 3, but showing the full time series of monthly means from 2010 to 2018 for SAN, ALF, TAB_TEF and RBA. Grey bands as in Extended Data Fig. 3, showing the 2010–2018 standard deviation for each month.

a)

ALF

Pearson's correlation   r: 0.68 and p: 0.046
Spearman's correlation r: 0.72 and p: 0.037
Kendall's correlation   r: 0.56 and p: 0.045
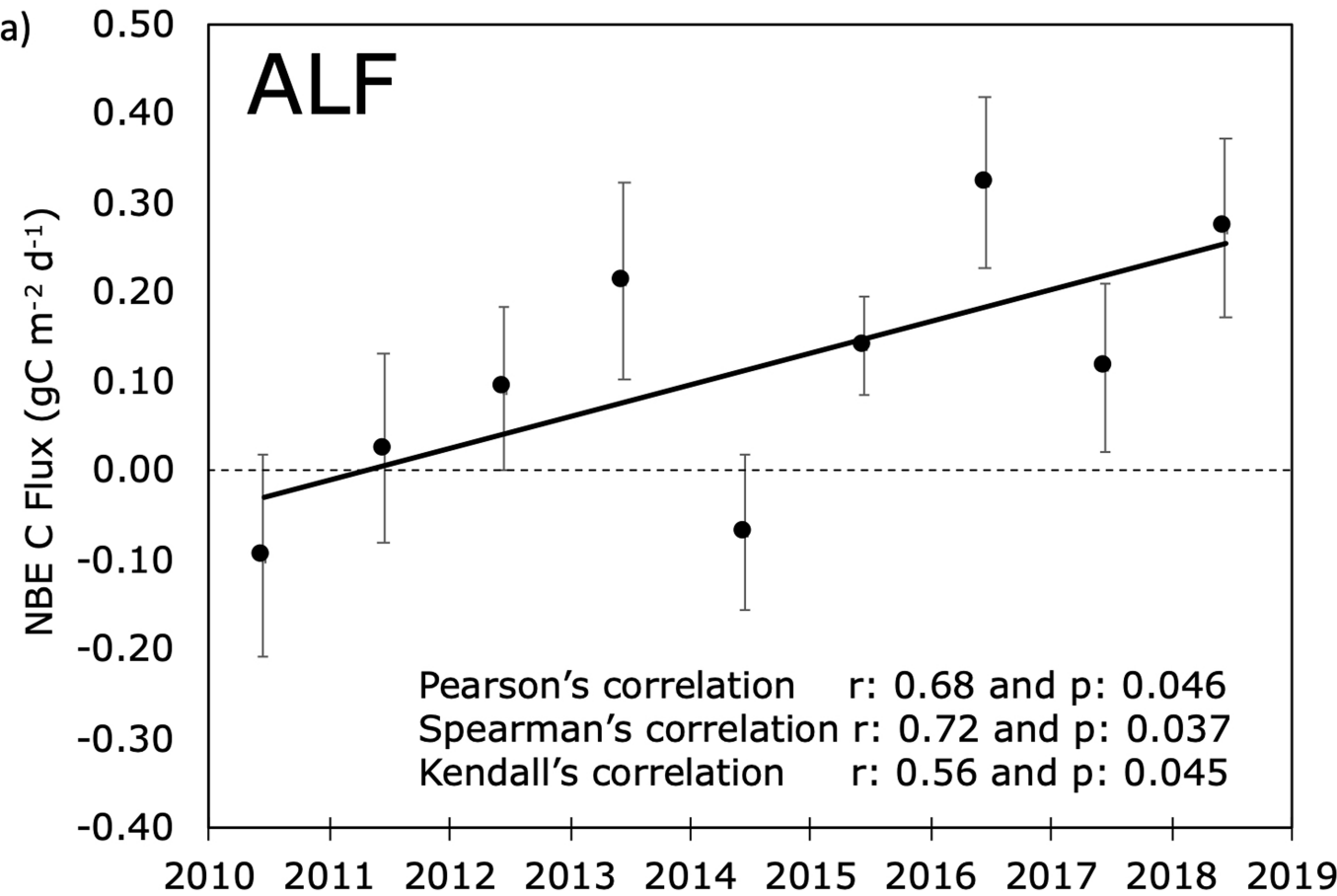
b)

	NBE $(gC\ m^{-2}d^{-1})$	Temp (°C)	GRACE (m)
2010	-0.10	27.48	-0.05
2011	0.02	27.28	-0.01
2012	0.09	26.79	-0.02
2013	0.21	26.76	0.00
2014	-0.07	27.17	0.02
2015	0.14	27.66	-0.09
2016	0.33	26.89	-0.22
2017	0.11	27.68	-0.07
2018	0.27	26.79	-0.04

Extended Data Fig. 5 | ALF NBE drivers. a, ALF annual mean NBE (NBE = total C flux − fire C flux, in g C m^{-2} d^{-1}) from 2010 to 2018. Error bars are uncertainties related to the background, travel time trajectories, emission ratios CO/CO$_2$ and natural CO flux (see Methods). **b**, Annual mean FC$_{NBE}$, annual mean temperature and GRACE (equivalent water thickness) satellite soil water storage anomalies.
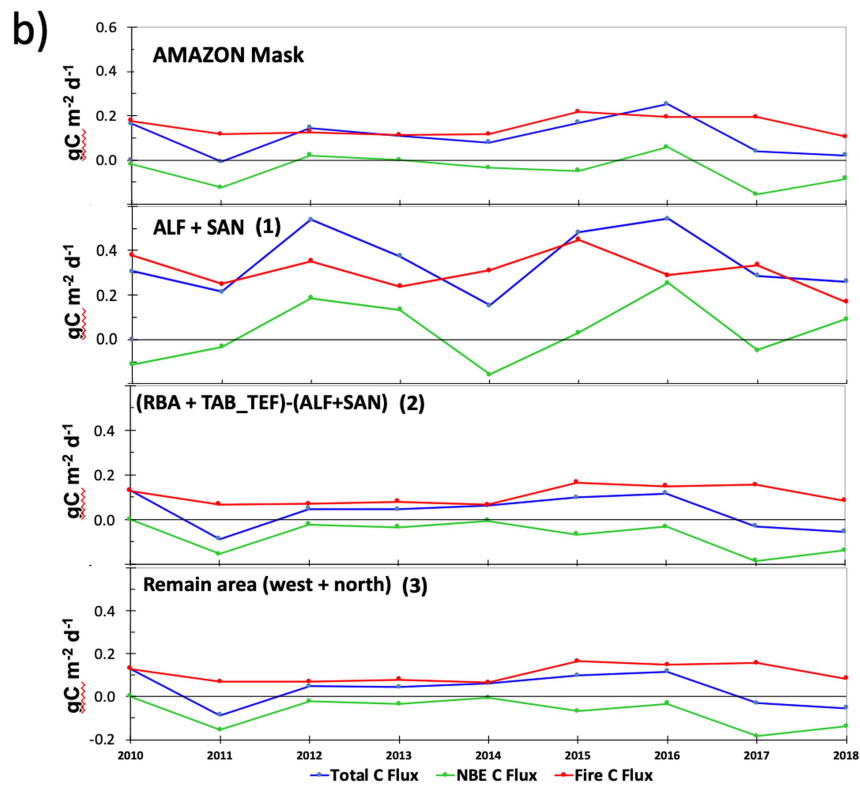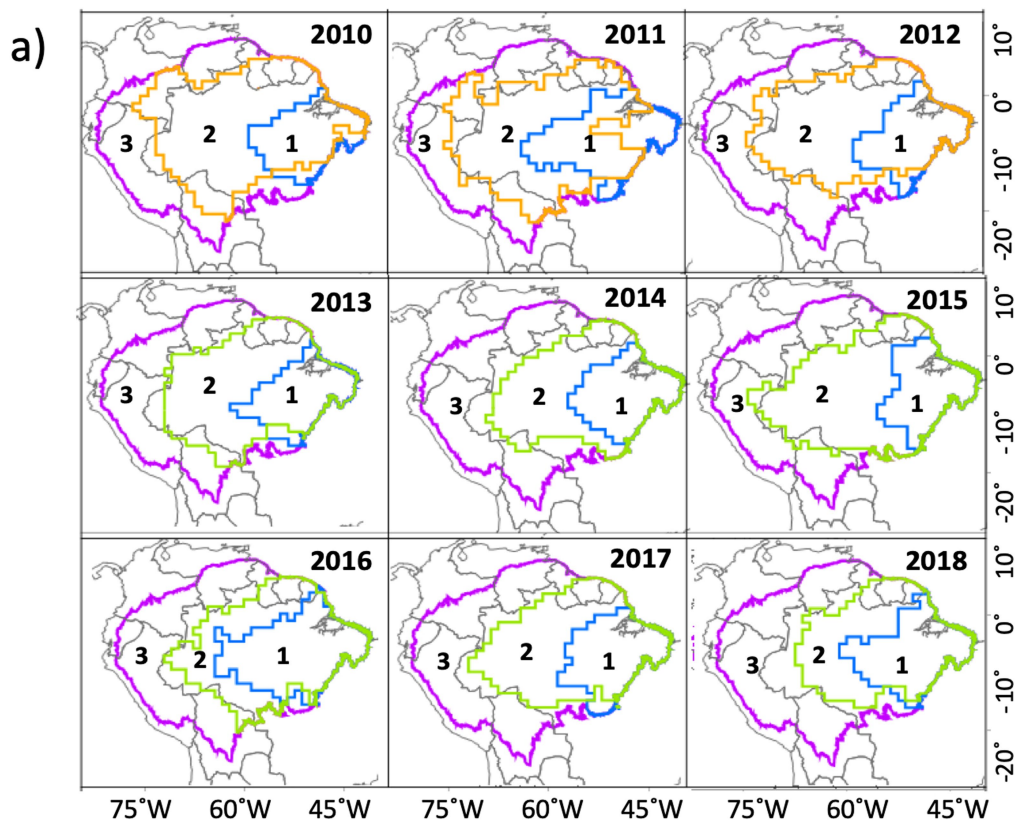
Extended Data Fig. 6 | Amazon carbon fluxes per region. a, Separation of three regions inside the Amazon Mask (7,256,362 km², purple line). Region 1: area of combined regions of influence for SAN and ALF; region 2: area of combined region of influence for RBA and TAB (2010–2012) and RBA and TEF (2013–2018), excluding region 1; region 3: the remaining area outside regions 1 and 2 and inside the purple line. **b**, Annual mean fluxes for regions 1, 2 and 3 (total, blue line; fire, red line; NBE, green line).
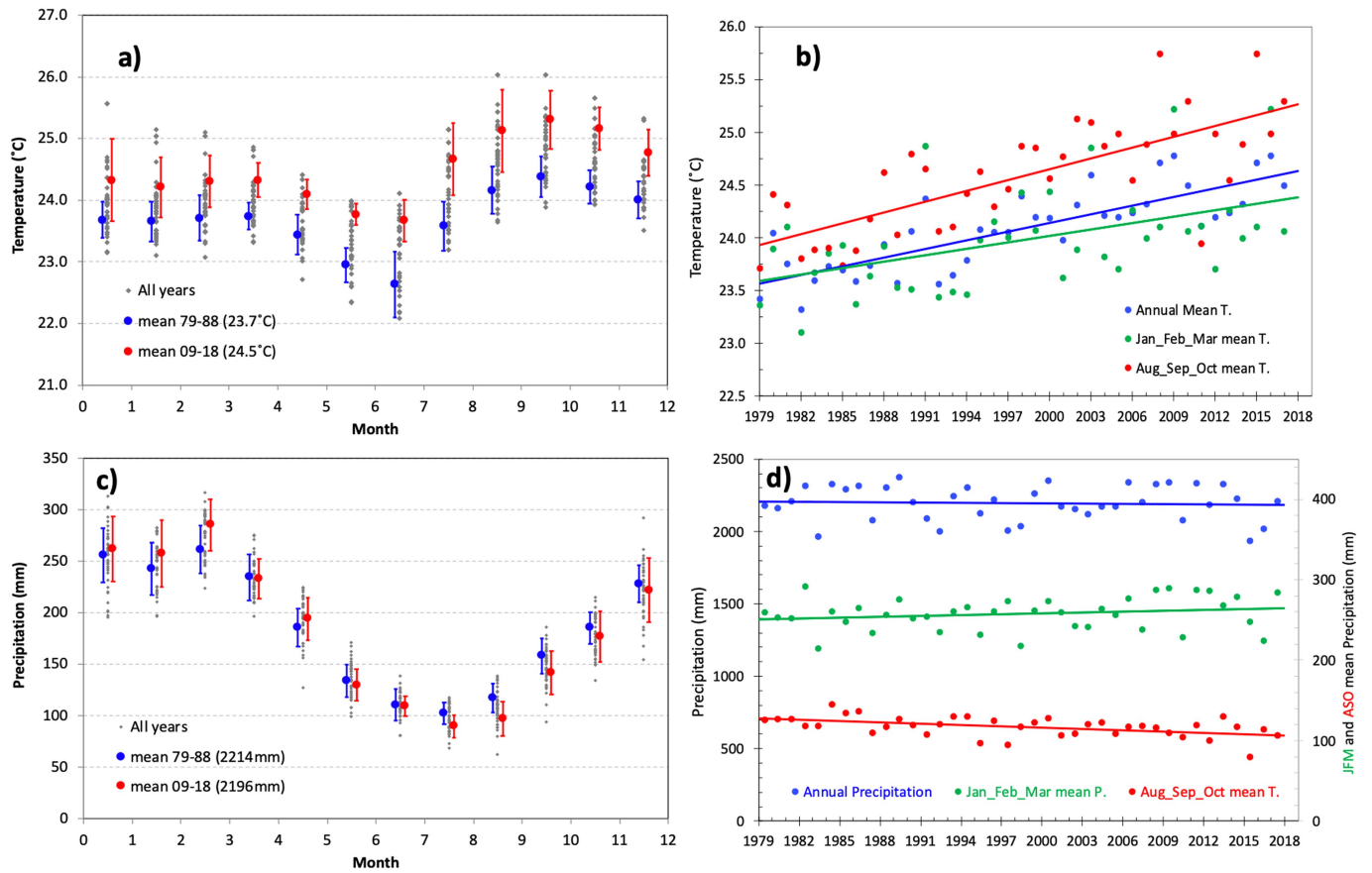
Extended Data Fig. 7 | Mean temperature and precipitation in Amazonia over the past 40 years. a, Monthly mean temperature in Amazonia in 1979–2018, calculated using ERA Interim (ECMWF) monthly means (see Methods). Grey points are monthly mean temperatures from 1979 to 2018. Blue and red circles show decadal monthly mean temperatures for 1979–1988 and 2009–2018, respectively. Error bars denote one standard deviation for the decade. **b,** Blue circles are annual mean temperatures; green circles show mean temperatures for January, February and March; red circles show mean temperatures for August, September and October. **c,** As in **a,** but for precipitation calculated using GPCP version 2.3 (see Methods). **d,** Blue circles are annual total precipitation; green circles are total precipitation for January, February and March; and red circles are total precipitation for August, September and October.
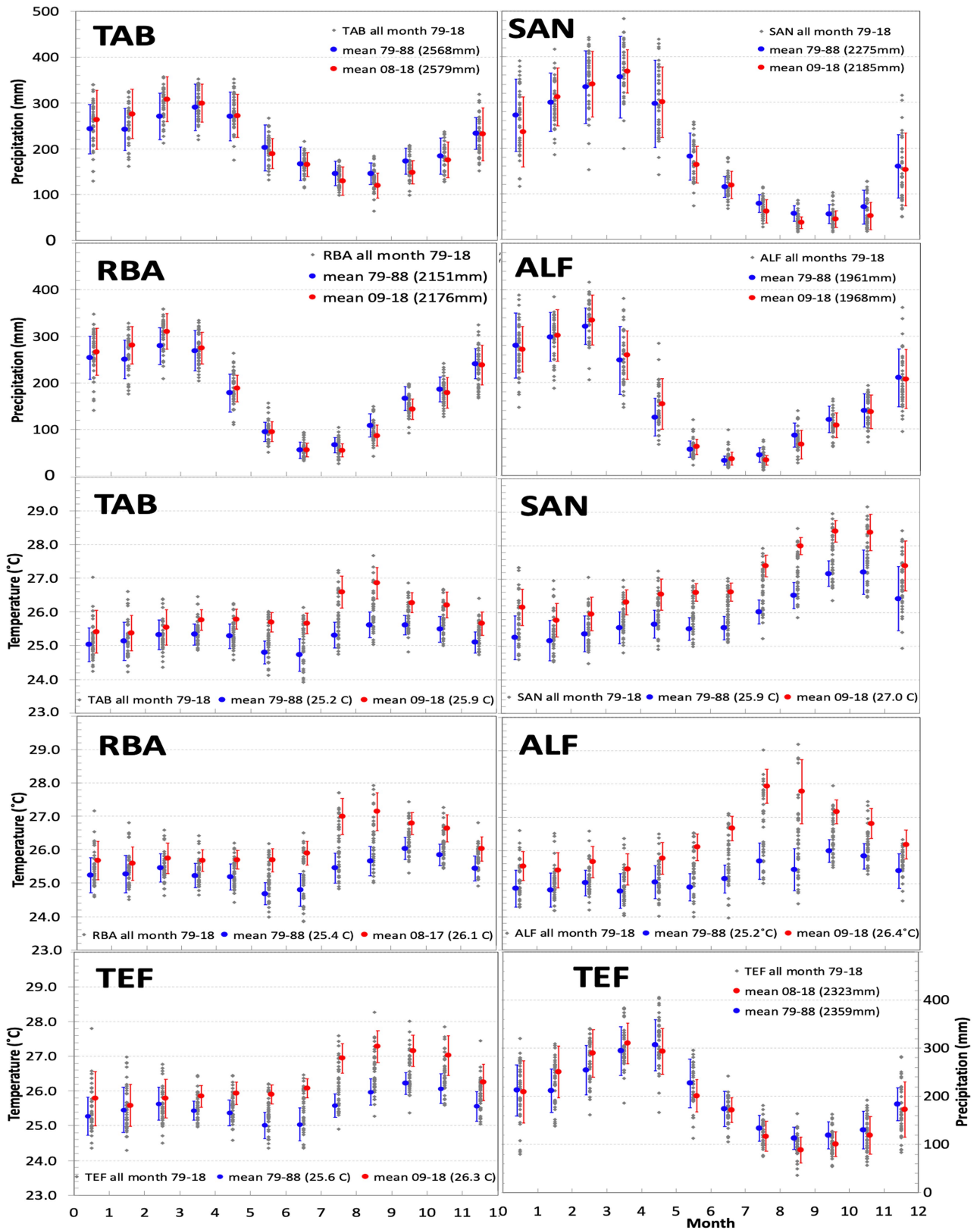
Extended Data Fig. 8 | Seasonal temperature and precipitation over the past 40 years. Monthly precipitation (GPCP v2.3) and monthly mean temperature (ERA-Interim) for TAB, SAN, RBA, ALF and TEF, calculated using spatial weightings from 2010–2018 quarterly regions of influence (Extended Data Fig. 2a) inside the Amazon mask. Symbols are as in Extended Data Fig. 7.

Extended Data Table 1 | Analysis of temperature and precipitation data obtained over the past 40 years

Temperature	period of time until actuality	Mean ASO		Annual Mean		Mean JFM	
		temperature increase (˚C)	annual growth rate (˚C/y)	temperature increase (˚C)	annual growth rate (˚C/y)	temperature increase (˚C)	annual growth rate (˚C/y)
Amazon CARBAM mask	40 years	1.37 ± 0.15	0.034 ± 0.004	1.02 ± 0.12	0.026 ± 0.003	0.82 ± 0.24	0.020 ± 0.006
ALF	40 years	2.54 ± 0.29	0.064 ± 0.007	1.46 ± 0.11	0.037 ± 0.003	0.87 ± 0.29	0.022 ± 0.007
	30 years		0.079 ± 0.009		0.051 ± 0.004		0.034 ± 0.006
	20 years		0.091 ± 0.017		0.061 ± 0.005		0.045 ± 0.007
SAN	40 years	1.86 ± 0.16	0.046 ± 0.004	1.38 ± 0.15	0.035 ± 0.004	1.00 ± 0.29	0.025 ± 0.007
	30 years		0.053 ± 0.005		0.042 ± 0.005		0.035 ± 0.008
	20 years		0.058 ± 0.005		0.050 ± 0.005		0.047 ± 0.009
TEF	40 years	1.61 ± 0.17	0.040 ± 0.004	1.08 ± 0.15	0.027 ± 0.004	0.54 ± 0.29	0.013 ± 0.007
	30 years		0.049 ± 0.007		0.039 ± 0.007		0.028 ± 0.011
	20 years		0.055 ± 0.011		0.047 ± 0.011		0.029 ± 0.022
RBA	40 years	1.72 ± 0.15	0.043 ± 0.004	1.06 ± 0.15	0.027 ± 0.004	0.57 ± 0.29	0.014 ± 0.007
	30 years		0.056 ± 0.004		0.037 ± 0.004		0.025 ± 0.007
	20 years		0.056 ± 0.004		0.041 ± 0.007		0.030 ± 0.015
TAB	40 years	1.45 ± 0.15	0.036 ± 0.004	0.94 ± 0.15	0.024 ± 0.004	0.67 ± 0.38	0.017 ± 0.009
	30 years		0.048 ± 0.007		0.035 ± 0.004		0.026 ± 0.011
	20 years		0.052 ± 0.011		0.039 ± 0.007		0.029 ± 0.018
Precipitation		Precipitation reduction (mm)	annual reduction rate (mm/y)	Precipitation change (mm)	annual rate (mm/y)	Precipitation change (mm)	annual rate (mm/y)
Amazon CARBAM mask	40 years	↓ 64 ± 19 (17%)	↓ 1.6 ± 0.5	↓ 27 ± 68 (NS)	NS	↑ 44 ± 34 (6%)	↑ 1.1 ± 0.9
ALF	40 years	↓ 60 ± 23 (24%)	↓ 1.5 ± 0.6	↑ 14 ± 36 (NS)	NS	↑ 22 ± 59 (NS)	NS
SAN	40 years	↓ 67 ± 23 (34%)	↓ 1.7 ± 0.6	↓ 208 ± 167 (9%)	↓ 5.2 ± 4.2	↓ 103 ± 81 (11%)	↓ 2.6 ± 2.0
TEF	40 years	↓ 72 ± 29 (20%)	↓ 1.8 ± 0.7	↓ 23 ± 125 (NS)	NS	↑ 59 ± 67 (NS)	NS
RBA	40 years	↓ 84 ± 33 (20%)	↓ 2.1 ± 0.8	↑ 30 ± 104 (NS)	NS	↑ 80 ± 49 (NS)	NS
TAB	40 years	↓ 77 ± 26 (16%)	↓ 1.9 ± 0.6	↑ 45 ± 95 (NS)	NS	↑ 102 ± 52 (14%)	↑ 2.5 ± 1.3

Observed trends from 1979–2018, where the monthly mean for each site was calculated using the quarterly mean region of influence from 2010–2018 as a spatial weighting function (Extended Data Fig. 2a; see Methods). The temperature and precipitation changes over 40 years were calculated using ordinary least-squares linear regression, and the reported uncertainty is based on the standard error of the slope; annual rates are reported only when the P value is lower than 0.05. The annual growth rate for temperature is accelerating, as can be seen by comparing the trends for the past 40, 30 and 20 years. Precipitation trends appeared constant over the 40 years analysed. Mean ASO is the mean for August, September and October and JFM for January, February and March. Precipitation is reported as totals for annual, ASO and JFM. NS (not significant) is reported for linear regressions with a P value higher than 0.05.

Extended Data Table 2 | Summary of the main results for ALF, SAN, RBA and TAB_TEF

Mean 2010—2018	ALF	SAN	RBA	TAB_TEF
Region of Influence (km^2)	1,484,117	703,621	3,515,577	2,917,132
Deforested Area[1,2] (km^2)	378,094 (26%)	206,614 (31%)	652,008 (13%)	191,232 (7%)[6]
Annual Burned Area per 1°x 1° cell[3,4] (km^2)	325 ± 220	168 ± 95	172 ± 100	108 ± 65
Annual Precipitation (mm)	1,937 ± 165	2,189 ± 151	2,115 ± 120	2,146 ± 186
Annual Mean Temperature (°C)	26.4 ± 0.3	27.0 ± 0.3	26.2 ± 0.7	26.2 ± 0.4
Peak Dry Season Change (79 - 18)				
Reduction in Precipitation in ASO (mm)	60.0 ± 23.8 (24%)	67.2 ± 23.1 (34%)	84.0 ± 33.1 (20%)	73.7 ± 27.8 (19%)[6]
Increase in Temperature in ASO (°C)	2.5 ± 0.3 (10%)	1.9 ± 0.2 (7%)	1.7 ± 0.2 (7%)	1.4 ± 0.2 (6%)[6]
Increase in Temperature in Aug_Sept (°C)	3.1 ± 0.3 (12%)	1.9 ± 0.2 (7%)	2.0 ± 0.3 (8%)	1.8 ± 0.2 (7%)[6]
Mean Flux 9 years (2010-2018)				
Total C Fluxes (gC m^{-2} d^{-1})	0.32 ± 0.09	0.41 ± 0.25	0.04 ± 0.11	0.03 ± 0.08
Fire C Fluxes (gC m^{-2} d^{-1})	0.20 ± 0.01	0.53 ± 0.03	0.14 ± 0.01	0.08 ± 0.01
NBE CFluxes (gC m^{-2} d^{-1})	+0.11 ± 0.09	-0.11 ± 0.26	-0.09± 0.11	-0.06 ± 0.08

Fluxes by Side east - west	SAN+ALF		RBA+TAB_TEF	
Total C Fluxes (gC m^{-2} d^{-1})	0.35 ± 0.11		0.04 ± 0.07	
Fire C Fluxes (gC m^{-2} d^{-1})	0.31 ± 0.01		0.11 ± 0.01	
NBE CFluxes (gC m^{-2} d^{-1})	+0.04 ± 0.11		-0.08 ± 0.07	

Amazon Carbon Fluxes (7,256,362 km^2)	Amazon Forest total Area
Total C Fluxes (gC m^{-2} d^{-1})	0.11 ± 0.15
Fire C Fluxes (gC m^{-2} d^{-1})	0.15 ± 0.02
NBE CFluxes (gC m^{-2} d^{-1})	-0.05 ± 0.15

Amazon Carbon Balance (7,256,362 km^2)	Amazon Forest total Area
Total C Balance (PgC y^{-1})	0.29 ± 0.40
Fire C Balance (PgC y^{-1})	0.41 ± 0.05
NBE C Balance (PgC y^{-1})	-0.12 ± 0.40

Deforested area, burned area, precipitation and temperature are all weighted according to the regions of influence. We observe a reduction in precipitation and an increase in temperature for ASO (August, September and October). Shown are the nine-year mean carbon flux (total, fire and NBE) from 2010 to 2018 and the uncertainty based on Monte Carlo analysis (see Methods), and weighted mean fluxes for SAN+ALF and RBA+TAB_TEF (see Methods). Amazon-wide C fluxes are reported in both g C m^{-2} d^{-1} and Pg C yr^{-1}. Values correspond to the interior of the Amazon mask (red line in Fig. 1) (7,256,362 km^2).

[1]PRODES products, obtained only inside the Brazil limit.
[2]The weighted cumulative historical deforested area was calculated using the density of trajectories per grid cell (see Methods).
[3]Annual burned area (km^2) – mean.
[4]Standard deviation.
[5]TAB_TEF: TAB (2010–2012) and TEF (2013–2018).
[6]Proportional mean according to the years of study.